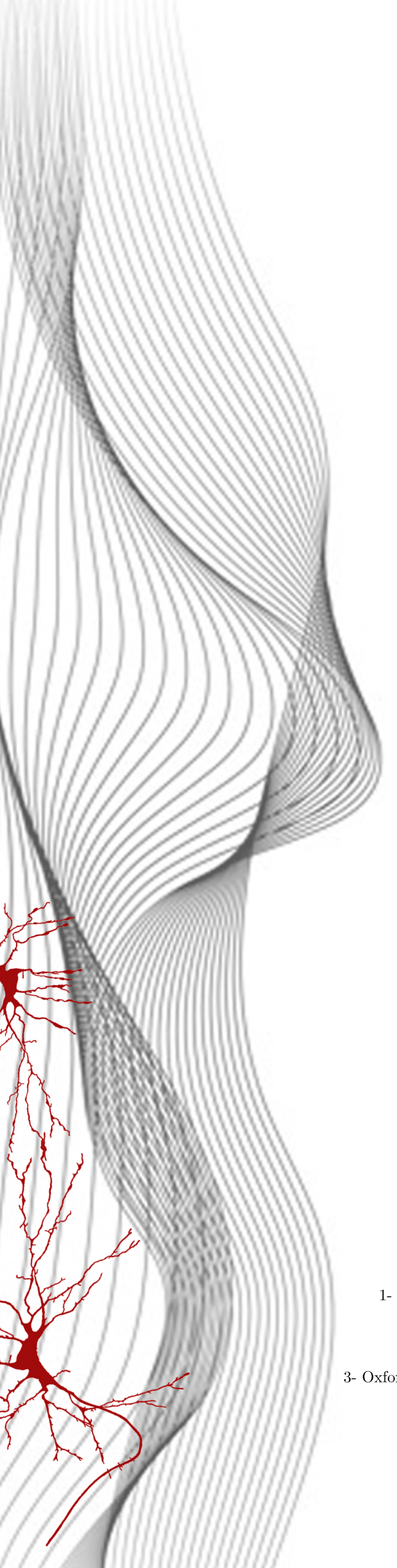

Time-Varying Temporal Functional Modes:

An instantaneous connectivity-based method that probes brain network reconfigurations while allowing for a shared anatomical infrastructure

MSc Thesis

Cognitive Neuroscience Research Master

Donders Graduate School, Radboud University

Tamara J. de Kloe[1,2]

Supervised by:

Alberto Llera Arenas[1,2]

Nils Kohn[1,2]

Christian F. Beckmann[1,2,3]

Second reader:

Maarten Mennes[1]

1- Donders Institute for Brain, Cognition and Behavior, Centre for Cognitive Neuroimaging

2- Department of Cognitive Neuroscience, Radboud University Medical Centre

3- Oxford Centre for Functional Magnetic Resonance Imaging of the Brain, University of Oxford

Abstract

The core cognitive neuroscientific aim is to determine how the brain gives rise to mental function. The answers provided to this ontological question depend, in part, on predominant methodology. Initial functional magnetic resonance imaging studies were mainly segregationist, i.e., focused on mapping psychological functions to individual brain sites. The modularity hypothesis underlying this approach, however, has been questioned since its conception. Conversely, it is argued that probing the neural underpinnings of mental function requires examination of interactions within and between integrated, spatially distributed functional brain networks. This is for example accomplished using functional connectivity methods, which examine co-variation of spatially distributed signals emitted from the brain. Time-averaged estimations of functional connectivity are commonly obtained, which assumes that the dependence structure between brain regions is constant over the course of an fMRI scan. In the past decennia, a line of research aims to probe time-varying functional connectivity changes of these networks, based on the premise that biologically meaningful changes in inter-regional relations are expected to occur. Available time-varying functional connectivity methods do not allow for spatial overlap, i.e., for functional networks to share a common anatomical infrastructure. This is addressed in Smith et al. (2012), where a spatial independent component analysis and a temporal decomposition are applied consecutively, resulting in so-called "Temporal Functional Modes" (TFMs). Classical TFM analysis is time-invariant, however, in the sense that the extent to which TFMs recruit specific spatial components (e.g. canonical functional connectivity networks) is assumed to be constant. To capture the time-varying nature of functional connectivity and simultaneously allow for spatial overlap, we developed a novel, time-varying version of classical TFM (TV-TFM) analysis. With this extension, we obtain moment-by-moment estimations of brain network reconfigurations, i.e. of how statistically independent temporal processes (i.e. TFMs) recruit statistically independent spatial components. Properties of the new model were explored by means of data simulations. Proof of principle for this new method was obtained by application to high temporal resolution fMRI data of participants performing a visuomotor association task. It was shown that the brain network reconfigurations captured with the new method closely followed the expectation based on the task design.

Keywords: time-varying functional connectivity, dynamic functional connectivity, independent component analysis, temporal functional modes, spatial overlap

Contents

> In science, the most important thing that has happened in the last forty years is the advance in instrumental design (...) a fresh instrument serves the same purpose as foreign travel; it shows things in unusual combinations. The gain is more than a mere addition; it is a transformation.
>
> – *Alfred North Whitehead, in Science and the Modern World (1926)*

1 Introduction

1.1 Integration vs. Segregation

Much like glasses through which one views the world, the choice of method critically determines the questions that can be asked and the limits of what can be observed in studying brain function. In the last few decades neuroimaging has become an essential tool for studying the temporal dynamics and spatial topology of the brain *in vivo*. The previous feature is usually studied using electroencephalography (EEG) and for the latter functional magnetic resonance imaging (fMRI) is the common method of choice, due to their relative high temporal and spatial resolution respectively (Bandettini, 2009; Rosa et al., 2010). Initial fMRI studies probed the neural substrates of brain function within a *segregationist* paradigm, focusing on mapping psychological function to individual activation sites. The corresponding methodological approach consists of per voxel comparisons of blood oxygen level-dependent (BOLD) signals to the expected time series, based on experimental designs ingeniously constructed to single out a cognitive function. Statistical tests on these comparisons provide maps which show what parts of the brain are associated with that particular cognitive function (Poldrack et al., 2011; Smith et al., 2004). Inherent to this mass-univariate approach is that voxels are studied *independently*, hence precluding examination of integration or collaboration. Since the discovery that spatially distinct and temporally synchronized brain regions can be differentiated in fMRI (Biswal et al., 1995), the field has started to characterize these integrated functional networks. A complementary *integrationist* approach is hence adopted, focused on characterizing integrated, spatially distributed functional brain networks and their role in cognition (Eickhoff & Muller 2015).

1.2 Methods for Studying Integration in fMRI

Integrated functional brain networks can be probed using functional connectivity methods. Popular methods such as seed-based correlation analysis (SCA; Biswal et al., 1995) and spatial ICA (Beckmann and Smith, 2004; Beckmann, 2012; McKeown and Sejnowski, 1998) have reliably differentiated these networks termed resting-state networks across participants (Beckmann et al., 2005; Damoiseaux et al., 2006), both in rest and during tasks (Smith et al., 2009). Alterations in functional connectivity of large-scale brain networks have proven to relate to cognition (e.g., Laird et al., 2011), behaviour (Rosazza and Minati, 2011), human development (Uddin, 2010), and personality (Mulders et al., 2018). They moreover show promise as a biomarker, as they relate to a variety of pathologies such as depression (Mulders et al., 2015; Greicius et al., 2007), schizophrenia (Lynall et al., 2010), and

Alzheimer's disease (Damoiseaux et al., 2012; Greicius et al., 2004; Lehmann et al., 2015; Lustig et al., 2003).

Functional connectivity is conceptually described as communication between brain areas to support cognitive function. Methodologically, it concerns statistical association between spatially distinct brain regions (Friston et al., 1993). The first described method, SCA, obtains correlations between a previously defined region of interest (ROI) or seed, and all other parts of the brain. This allows for hypothesis-driven analyses, as it probes whole-brain connectivity of an area that for example has previously been related to a particular cognitive function. This approach, however, restricts the analysis to one chosen region or system, although connectivity changes between other regions might occur (Bijsterbosch, 2017). The second method, spatial ICA, is a multivariate and model-free blind source separation technique that assumes that the fMRI signal consists of a linear combination or mixture of signals from different sources. The signals are decomposed ('unmixed') into a set of spatial components that are statistically maximally independent, by extracting non-gaussian sources (Beckmann and Smith, 2004; Beckmann et al., 2005; Beckmann, 2012). The extracted components are generally understood as brain networks that show similar BOLD activity (McKeown, 2003). The data can also be decomposed in temporally independent sources by means of temporal ICA. Of the two, spatial ICA is more common in fMRI. An important reason for this is that in fMRI the spatial dimension is generally much larger than the temporal dimension, i.e. more voxels than volumes are obtained (Smith et al., 2012; Calhoun et al., 2001). In either case, the sources or components are described by means of a spatial map and a corresponding time series. Both these spatial and temporal features can subsequently be related to behaviour, or be compared between certain groups of individuals. Almost all available ICA-based functional connectivity studies are performed in resting-state. In part because this does not provide a behavioural benchmark to which the time series can be related, like in task-based fMRI, the gold standard is to statistically compare the spatial maps across individuals or groups, e.g. to inform on significant differences in strength, shape or location of the networks (Bijsterbosch et al., 2018).

1.3 Time-varying functional connectivity

1.3.1 Rationale.

Most functional connectivity methods assume that the dependence structure between brain regions is constant over the course of an fMRI scan. In SCA, for example, average correlations between BOLD signals of specific seed- and target regions over an entire scan duration or condition are used as a proxy for the network behaviour. In spatial ICA, the spatial map weights, i.e., the connection strengths between regions, are constant over time (Hutchison et al., 2013). Many significant advances have been made in understanding large-scale brain networks while working under this assumption. A recent line of research posits that it, however, fails to capture the expected changes in interactions between, or shifts in dominance of, large-scale brain networks (Liégeois et al., 2017, 2019; Lurie et al., 2020; Preti et al., 2017). It is argued that characterisation of time-varying FC metrics is hence required, i.e. time-varying changes in *integration* of spatially distributed functional brain networks should be examined. The term often used in the literature is "dynamic functional

connectivity" (Preti et al., 2017). In a recent joint article by various leading experts in this developing field (Lurie et al., 2020), it was argued that standardisation of terminology is paramount. "Time-varying functional connectivity" (TVFC) was proposed, as differences between disciplines in use and definitions of the term "dynamic" can cause ambiguity. Conceptually, TVFC is defined as functional connectivity that varies as a function of time, and hence concerns temporal reconfiguration of functional entities (Iraji et al., 2020). Methodologically, it means that the parameters used to describe the dependence structure between these functional entities vary across time. It was pointed out that TVFC is broader than the static–dynamic distinction, whereas this has previously (mistakingly) been taken to mean the same thing (Lurie et al., 2020). Not every TVFC metric implies non-stationarity, which is defined by a non-constant mean and covariance (and all other higher-order moments; Hutchison et al., 2013). Conversely, Liégeois et al. (2017) showed that certain TVFC processes fall within the space of stationary models.

1.3.2 Time-varying functional connectivity methods.

A range of TVFC methods has been suggested in recent years, which differ in several aspects. First, a distinction can be made between methods that explicitly model the underlying neural processes (i.e., dynamic biophysical models; the orange arrows in Figure 1) and those that characterise the time-resolved dependence structure from the BOLD signals (the green and blue arrows in Figure 1). A first important differentiation between methods of the latter category is the temporal window that is considered, ranging from individual frames or time-points (i.e. instantaneous connectivity) to larger time windows (Preti et al., 2017)). The functional connectivity metrics that are obtained per time-point or window are either directly summarized using graph-theoretic measures, or "brain-states" are estimated using matrix factorization techniques (e.g., k-means clustering, or PCA). These brain states are subsequently described using time-varying parameters such as transition probabilities and dwell times (Lurie et al., 2020; Preti et al., 2017).

1.3.2.1 Sliding-window approaches.

Most methods that characterise the time-resolved dependence structure directly from the BOLD signals are variations of the sliding-window pairwise correlation approach (for a review see Preti et al., 2017; the green arrows in Figure 1). In its most rudimentary form, this consists of segmenting the entire scan duration into smaller windows and computing a functional connectivity metric over successive (overlapping or non-overlapping) windows (Preti et al., 2017). Many extensions of this framework have been proposed, aiming to deal with the strong objection that window type and length have a substantial impact on the characterisation of the functional dynamics. On the one hand, small windows can introduce spurious correlations because of insufficient information to estimate TVFC robustly (Leonardi and Van De Ville, 2015). Given the inverse relationship between periodicity and frequency, another problem is that short windows by definition only allow probing high frequencies. Although there is some evidence that resting-state networks are broadband processes (van Oort et al., 2012; Niazy et al., 2011), they are generally assumed to be dominated by low-frequency oscillations (around .015Hz, Niazy et al., 2011) which will appear constant for short time-windows. Large windows, on the other hand, smooth out the time-varying

properties of interest (Hindriks et al., 2016; Iraji et al., 2020). A multivariate, ICA-based, approach to sliding-window analysis has also been suggested (Kiviniemi et al., 2011). Performing spatial ICA on a sliding-window basis results in a set of independent components per window. Using this approach to analyse Default Mode Network (DMN) activity, Kiviniemi et al. (2011) concluded that DMN subnetworks dynamically change interactions throughout a full acquisition length and that activity of the whole DMN network (as identified by stationary ICA) never occurs. Splitting of the DMN network into multiple sub-networks is, however, known to depend on the dimensionality of the ICA. A second objection to this multivariate ICA-based sliding window approach is that components need to be matched across windows, which is problematic since the order of components extracted using ICA is relatively arbitrary (Bijsterbosch, 2017).

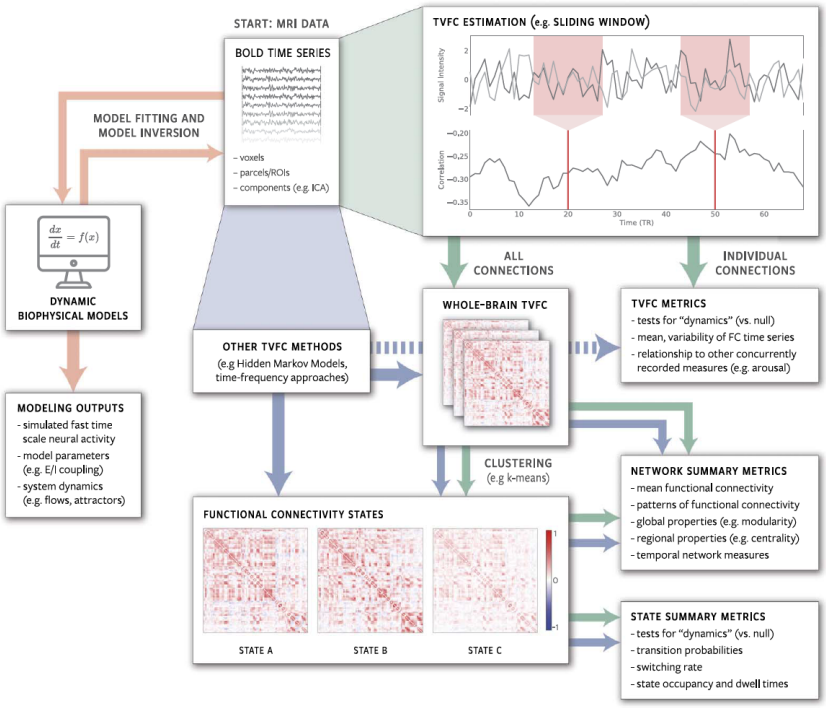

Figure 1. Schematic illustration of common TVFC analysis and modelling approaches: orange arrows indicate the workflow for dynamic biophysical models; green arrows indicate a typical sliding-window based workflow, and blue arrows represent alternative approaches taken (image taken from Lurie et al., 2020).

1.3.2.2 Time-frequency approaches.

The seminal approach in electrophysiology called time-frequency analysis has also been applied to TVFC. It explores connectivity at multiple frequencies and circumvents the described window constraints of sliding window approaches. The seminal time-frequency approach to TVFC in fMRI is Wavelet Transform Coherence (Chang and Glover, 2010), where the size of the "window", i.e., the wavelet, is adjusted based on the time-scale of the frequencies under inspection. Time-frequency analyses result in a description of the amount of joint power between two time series and their relative phase as a function of time and frequency. Using this approach, it has been found that within- and between network connectivity patterns differ across frequencies, suggesting the presence of overlapping interactions that are potentially

averaged in classical approaches (Chang and Glover, 2010; Yaesoubi et al., 2015). A longstanding idea is that low frequency, slow-wave signals drive resting-state networks. Probing their spectral characteristics using a Hilbert-Huang transform, Niazy et al. (2011) found that although low-frequency signals indeed dominate resting-state networks, they are characterized by different frequencies at different levels of phase synchrony. That is, they were found to be broadband processes. Leading Eigenvector Decomposition Analysis (LEiDA, Cabral et al., 2017) focuses specifically on phase-coherence of the BOLD signals, where the phases are obtained using a Hilbert Transform (Deco and Kringelbach, 2016; Deco et al., 2017; Glerean et al., 2012). Identifying TVFC states is done according to the BOLD phase relative to the leading eigenvector (i.e. largest magnitude) which captures the dominant pattern of functional connectivity per time point. Focusing on the leading eigenvector per time point deals with the main objection raised against time-frequency approaches: that the output is very extensive, which limits interpretability (Hutchison et al., 2013).

1.3.2.3 Point-process and co-activation approaches.

Point-process analysis assumes that all relevant information about TVFC can be extracted from short periods where BOLD signals exceed a certain threshold (Petridou et al., 2013; Tagliazucchi et al., 2016). The metric of interest here is the number of co-activations between voxels, defined by simultaneously crossing the threshold. The selection of this threshold is, however, arbitrary. Liu and Duyn (2013) suggested to only use frames where a seed time-course exceeded the threshold. Moreover, where the metric in the original method was binary (exceeded vs not exceeded), they suggested clustering the original fMRI volumes obtained at those frames generating so-called co-activation patterns (CAPs). This brings us to a second major differentiation between TVFC methods (in addition to the time frame considered), namely whether the temporal ordering of the data is considered. Some methods ignore temporal structure altogether, e.g. clustering applied to obtain CAPs which treats time points interchangeably. Other TVFC approaches make use of the temporal structure at some stages of the analysis, e.g. in estimating the phase-coherence of BOLD in LEiDA, but ignore it at other stages, e.g. by subsequently applying k-means clustering (Cabral et al., 2017; Lurie et al., 2020).

1.3.2.4 Modeling approaches.

Another line of TVFC methods aims not just to estimate time-varying functional connectivity fluctuations over time, but to explicitly model to temporal structure (Preti et al., 2017). Promising approaches of this sort fit multivariate dynamic models, i.e., Hidden Markov Models (HMMs; Vidaurre et al., 2016, 2017) or autoregressive models (AR-1; Rogers et al., 2010) to fMRI time series. The most crucial difference being that HMMs assume the existence of discrete brain states, whereas AR-1 models are continuous, such that each time point is modelled as a linear combination of the previous ones. The latter approach was recently shown to more adequately capture task-based phenotypes than time-averaged functional connectivity measures (Liégeois et al., 2019), illustrating the potential added value of TVFC over time-averaged approaches.

Given the high dimensionality of TVFC data, previously discussed dimensionality reductions are performed in the temporal domain (resulting in loss of information on the

temporal ordering of the data). Most methods also start with a dimensionality reduction in the spatial domain, called a parcellation. Instead of analyzing the temporal properties based on voxel time series directly, the voxels are first summarized at a lower dimensionality. That is, voxels are grouped into brain regions which are functionally or anatomically similar. This procedure typically results in a set of completely separate brain regions, i.e. there is no overlap between them (called a "hard parcellation"), or in regions that have very little overlap (called a "soft parcellation"). For functional parcellations, this implies that a one-to-one mapping between cortical structure and brain function is assumed. In other words, a brain region is expected to be recruited by one functional entity only. There is no (or very little) spatial overlap.

1.4 Allowing for Spatial Overlap: TFM Analysis

The lack of accounting for spatial overlap was formulated by Friston (1998) in a critique on spatial ICA. He argued that by inducing orthogonality in the spatial domain, it is assumed that functional networks do not share underlying anatomical structure. Such spatial overlap is, however, expected: first, because functional sub-units within certain regions are not separable due to the limited spatial resolution of fMRI data, and second because certain areas supposedly participate in more than one functional network. In response, it was posited that a similar limitation occurs when enforcing orthogonality in the temporal domain due to stimulus correlated effects (e.g., motion related to the presented stimuli), and that spatial ICA provides relatively adequate representations when spatial overlap occurs in the presence of noise (which is inherent to fMRI data; Beckmann et al., 2005). The amount of spatial overlap that spatial ICA allows for is, however, limited (Bijsterbosch, 2017). Not allowing for spatial overlap can obscure the actual functional organization of the brain, in the words of Smith et al. (2012) because: "if two regions participate in multiple functional networks, their apparent temporal correlation will reflect the combined contribution from all networks, obscuring the true underlying functional organization. The correlation will not necessarily be meaningful, being some unknown combination of correlations caused by various distinct processes". Smith et al. (2012) therefore addressed this by subsequently applying a spatial ICA and a temporal ICA decomposition. Time series of resting-state networks are hence further decomposed ('unmixed'), into a set of temporally independent components called "Temporal Functional Modes" (TFMs). Employing TFM analysis, it was found that well-established resting-state networks, e.g., the DMN, involve different functional sub-processes that overlap spatially (Smith et al., 2012).

This approach has hitherto not widely been used because it requires an enormous number of samples, not generally available in fMRI studies. In the original TFM study, 36 scans of 10 minutes (obtained from five participants) were concatenated before running the analysis (Smith et al., 2012). Recently, TFMs were obtained at the single-subject level for the first time using an ultra-fast imaging sequence (Gomez et al., 2020). This provides the opportunity to examine whether inter-individual differences in TFMs relate to psychiatric and behavioural measures. Gomez et al. (2020) performed TFM analysis both on resting-state data and on task-based data of participants performing a visuomotor association task. They

found that reproducible TFMs can be found at the individual subject level. Similar TFMs were identified independent of the original spatial dimensionality reduction, and they were deemed largely free from confound contamination. Six TFMs were identified across most participants and scans, the most common of which consisted of an anti-correlated pattern between the DMN and task-positive networks termed the "default temporal mode". Another common TFM supposedly involved in sensory integration recruited the DMN, task-control and executive control networks in anti-correlation with the auditory network, somatosensory network and visual networks among others. Compared to resting-state, task activity induced small changes in the networks, but these were overshadowed by inter-individual differences.

1.5 TV-TFM Analysis

Classical TFM analysis is considered a TV-TFM method by some, given that activity at each time point is considered as a linear combination of resting-state network activity (Preti et al., 2017). Classical TFM analysis is, however, *time-invariant* in the sense that the extent to which TFMs recruit specific spatial components (e.g. canonical functional connectivity networks) is assumed to be constant. To capture these time-varying changes and allow for spatial overlap simultaneously, *we developed a novel, time-varying version of classical TFM (TV-TFM) analysis.* With this extension we obtain moment-by-moment estimations of brain network reconfigurations, that is of how statistically independent temporal processes (i.e., TFMs) recruit statistically independent spatial components. In the current study, the properties of the new model are explored by means of data simulations and a proof of principle is obtained by applying TV-TFM analysis to high temporal resolution fMRI data of participants performing a visuomotor association task.

2 Methods

2.1 TV-TFM analysis pipeline

In the current study, we extended classical TFM analysis to obtain moment-by-moment estimations of brain network reconfigurations while simultaneously allowing for spatial overlap. Traditional TFM analysis consists of two stages: a spatial decomposition to retrieve canonical resting-state networks, and a subsequent temporal decomposition to retrieve TFMs (see Figure 2 for a visual representation).

2.1.1 TFM stage 1: obtain (canonical) resting-state networks.

As previously described, a popular tool for the first stage is spatial ICA. To identify a set of spatial building blocks, preprocessed fMRI data with v voxels measured at t time points are decomposed into a set of statistically independent components (d). That is, a two-dimensional ($v \times t$) fMRI data matrix (X) is approximated by a set of spatially independent non-Gaussian sources, which are described as spatial maps (S, of dimensions: $v \times d$) and their associated time courses (T, of dimensions: $d \times t$):

$$X_{v \times t} = S_{v \times d} \times T_{d \times t} + \epsilon_{tfm_1} \tag{1}$$

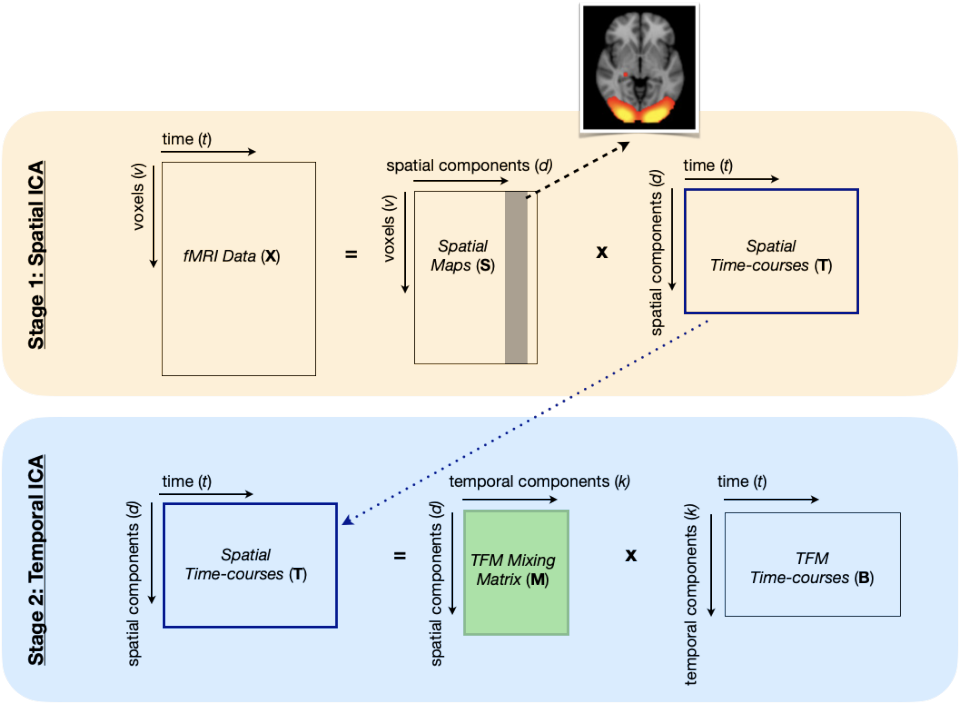

Figure 2. A schematic representation of TFM analysis. Image adapted from Bijsterbosch (2017). The brain image of a spatial component was taken from Smith et al. (2009).

Obtaining resting-state networks by means of spatial ICA can be done in different ways. First, spatial ICA can be applied at the single-subject level, which results in a description of *subject-specific* functional connectivity networks. Applying ICA at the single-subject level is problematic when the goal is to compare across participants, because of the correspondence problem. That is, slight variations in the data can cause differential splitting of components, such that one component in one participant can be split into multiple components for another participant. This precludes matching of components across different datasets. To overcome this, a group-level ICA can be performed followed by the dual-regression technique (Beckmann et al., 2009; Nickerson et al., 2017). Participant-specific maps and time series are obtained here, by means of two multiple regression analyses within a general linear model framework. First, individual subject's time series are estimated by regressing the group ICA network template onto the individual participants' pre-processed fMRI data (i.e. spatial regression):

$$X_{v\times t} = \hat{\hat{S}}_{v\times d} \times T_{d\times t} + \epsilon_{dr_1} \tag{2}$$

with:

$$pinv(\hat{\hat{S}})_{d\times v} \times X_{v\times t} = T_{d\times t} \tag{3}$$

where, T reflects the average time-course related to a specific network component of the template ($\hat{\hat{S}}$), after considering the contributions of the other components to that time series. The subject-specific time courses estimated in equation (3) are then used as predictors in a second multiple, temporal regression to estimate the subject-specific spatial maps:

$$X_{v\times t} = S_{v\times d} \times T_{d\times t} + \epsilon_{dr_2} \tag{4}$$

with:

$$X_{v\times t} \times pinv(T)_{t\times d} = S_{v\times d} \quad (5)$$

With group-ICA and dual-regression, individual subject maps and time series are estimated with respect to *group or sample-specific* connectivity networks. Instead of group-specific templates, previously established functional (or anatomical) templates can also be used (Nickerson et al., 2017). This approach is taken in the current study: a dual-regression analysis is performed using templates of major brain networks identified in resting-state by means of group spatial ICA, which have been shown to correspond to networks identified from a large set of task-based brain activation studies (Smith et al., 2009). The latter finding provides support for the robust occurrence of these spatial networks, both in rest and during task. For constructing the templates, group-ICA was performed at a dimensionality of 20 to examine large-scale brain networks (SMITH20 template), and a higher dimensionality of 70 (SMITH70 template) to probe a lower level of the functional hierarchy (i.e. subnetworks). Of the 20 components identified with the previous, ten were well-defined and clearly overlapping the networks identified in task-based data. In the current study, dual-regression was performed using both the SMITH20 and SMITH70 templates. As previously described, Gomez et al. (2020) found that similar TFMs can be extracted across different functional (or anatomical) spatial decompositions. The SMITH20 spatial template was hence chosen for illustrative purposes in the rest of this paper because the included networks are better defined, which aids interpretability.

2.1.2 TFM stage 2: obtain temporal functional modes.

In classical TFM analysis, the second stage consists of applying temporal ICA to the time series retrieved in the first step, decomposing them into a set of statistically independent TFMs (k). That is, the spatial ICA time series $T_{t\times d}$ are approximated by a set of *temporally independent* non-Gaussian sources, which are described as a product of the TFM mixing matrix (M, of dimensions: $d \times k$) and the associated temporally independent time series (B, of dimensions: $k \times t$):

$$T_{d\times t} = M_{d\times k} \times B_{k\times t} + \epsilon_{tfm} \quad (6)$$

Classical TFM analysis thus describes the preprocessed fMRI data as a product of three matrices: the spatial ICA spatial maps, the TFM mixing matrix (which describes how the temporal components weigh onto the spatial components), and the TFM associated time courses:

$$X_{v\times t} = S_{v\times d} \times M_{d\times k} \times B_{k\times t} + \epsilon_{total} \quad (7)$$

The temporal ICA at stage two was performed with a dimensionality of 21 in the original Smith et al. (2012) paper and at dimensionalities 8, 15, and 21 at the single-subject level by Gomez et al. (2020). Ensuring a lower dimensionality for the temporal–than for the spatial decomposition (i.e. smaller than the spatial ICA matrix rank) in the current study we ran temporal ICA at the following dimensionalities: 8,10 and 15 for the SMITH20 template, and 8, 10, 15, and 21 for the SMITH70 template. The main results described in the current paper stem from the highest model order, i.e. 15, for the better defined SMITH20 template.

2.1.3 TV-TFM analysis: obtain time-varying temporal functional modes.

As described in equations (6) and (7), in classical TFM analysis a time-averaged mixing matrix is obtained. In other words, the extent to which TFMs recruit specific spatial components (e.g. canonical functional connectivity networks) is assumed to be constant. In the current study, classical TFM analysis is extended as to include moment-by-moment estimations of the extent to which TFMs recruit different spatial components. That is, a time-varying TFM (TV-TFM) mixing matrix is obtained (see Figure 3 for a visual representation).

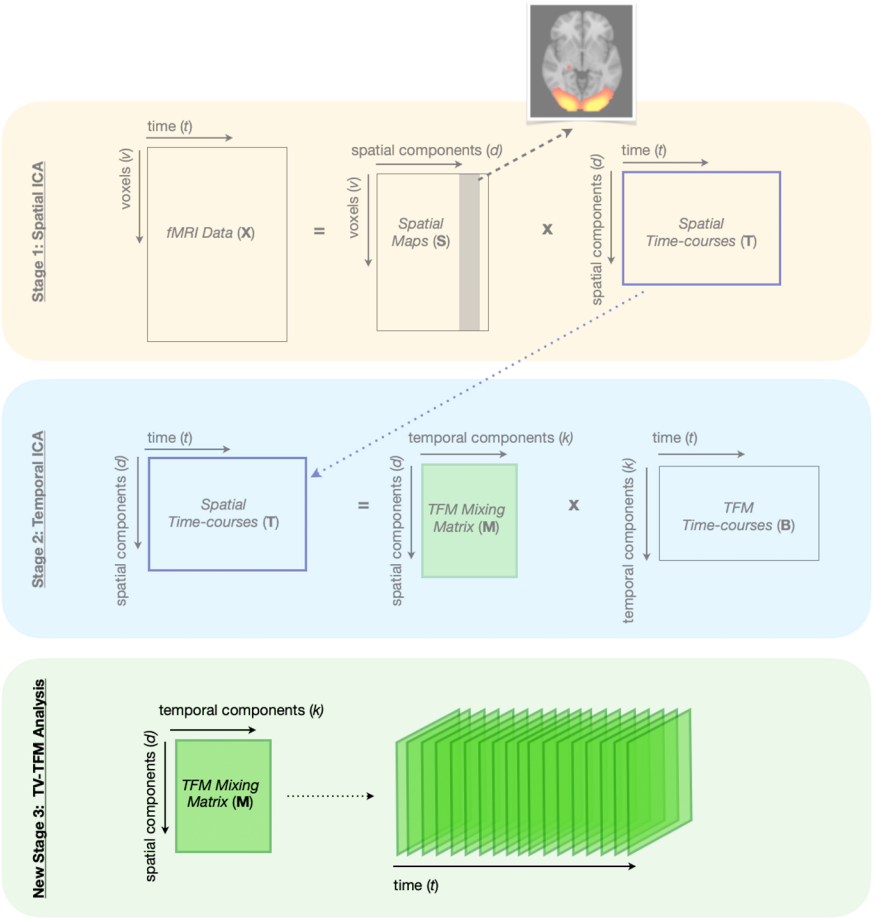

Figure 3. A schematic representation of the new extension of TFM analysis. In stage 3, a TV-TFM mixing matrix is retrieved.

Consider the noise-free TFM model of preprocessed fMRI data as described in equation 7 (in the presence of noise substitute X by $X - \epsilon_{total}$):

$$X = SMB \tag{7}$$

where S, M and B were previously defined as the spatial maps, the TFM mixing matrix and the TFM time series respectively. Given equation (7), the TFM mixing matrix M can be described as:

$$M = AXB^{\intercal}Z \tag{8}$$

where $A := pinv(S)$, $Z := (BB^\intercal)^{-1}$ and the product of $B^\intercal$ and Z amounts to the right pseudo-inverse.

Note that the only time-dependent quantities in equation (8) are $X \in \mathcal{M}_{v\times t}$ and $B^\intercal \in \mathcal{M}_{t\times k}$. Considering the product between $X \in \mathcal{M}_{v\times t}$ and $B^\intercal \in \mathcal{M}_{t\times k}$ in equation (8) as a sum over time:

$$M = AXB^\intercal Z = A\left(\sum_{t=1}^{T} X(t)B^\intercal(t)\right)Z = \sum_{t=1}^{T} AX(t)B^\intercal(t)Z \tag{9}$$

where $X(t) \in \mathcal{M}_{v\times 1}$, $B^\intercal(t) \in \mathcal{M}_{1\times k}$, and:

$$M_t(t) := AX(t)B^\intercal(t)Z. \tag{10}$$

M can be obtained by summing over the time dimension of this time dependent quantity, namely:

$$M = \sum_{t=1}^{T} M_t(t). \tag{11}$$

Note that for normalized (mean zero and unit standard deviation) X and $B^\intercal$ time series, $M_t(t)$ describes a scaled version (through Z, i.e. the covariance of B) of the instantaneous correlation (van Oort et al., 2018) between $A \times X$ and $B^\intercal$ at time t. That is, the instantaneous correlation between the spatial maps regressed onto the preprocessed fMRI data (i.e. $A \times X(t)$) and the TFM time series ($B^\intercal(t)$).

Defining a function:

$$f(t) := NM_t(t) \tag{12}$$

we have that:

$$M = \frac{1}{N}\sum_{t=1}^{T} f(t) \tag{13}$$

As shown in 13, the function f is a scaled version of M_t such that M is the *time-average* of the instantaneous correlation between $A \times X$ and $B^\intercal$ scaled by its covariance.

A python package was developed which allows to simulate data for TV-TFM analysis and to run TV-TFM analysis on (task-based) fMRI data. The package will be made available on https://github.com/tamarajedidja/tv-tfm upon publication.

2.2 Datasets

Properties of the new model were examined by applying TV-TFM analysis to simulated data. TV-TFM analysis was subsequently applied to high temporal resolution fMRI data of participants performing three runs of a visuomotor association task, previously collected by Z. Fazal.[1]

[1] The original plan was to collect data using an ultrafast fMRI sequence (MESH). Due to the current COVID-19 situation, I was not able to collect these data. Experience with data collection was however gained in the first year of the CNS master when I performed recruitment and data collection for the 13th wave of the BIBO longitudinal study within the Affective Neuroscience Lab at the Donders Institute, and for which I became a certified MRI user.

2.2.1 Synthetic data.

A highly simplified proxy of single-subject data was simulated, to probe properties of the TV-TFM model (rather than explicitly testing the model, or representing fine-grained, biologically plausible details). As visually presented in Figure 4, we induced different structures in entries of simulated time-varying mixing matrices, $M_t \in \mathcal{M}_{2\times 2\times T}$, where T describes the number of time points. That is, i.e. step-functions, square wave signals, and sinusoids were induced along the time-dimension. For one entry, this conceptually corresponds to a TFM mode recruiting a certain resting-state network for half the duration (step-function), or alternatively (square wave signal and similarly, due to its smooth transitions, for the more biologically plausible sinusoid). The product of M_t and $B \in \mathcal{M}_{2\times t}$, i.e. two Laplace distributed time series, per timepoint provided a reconstruction of X, to which a normally distributed random noise factor was added. Note that for sake of simplicity, the first spatial decomposition stage was eliminated (herewith excluding S). Temporal ICA (stage 2) and TV-TFM analysis (stage 3) were subsequently applied to X, to obtain the estimated $\hat{B}$ and $\hat{M}_t$. Two conditions of interest were examined. First, anti-correlated structures were induced in entries of M_t which belonged to different TFMs as identified by temporal ICA, but to the same resting-state network. This resembles a situation in which this resting-state network participates in different temporally independent processes. Second, anti-correlated structures were induced in entries of M_t belonging to the same temporally independent process, but to different resting-state networks. The goal was to probe if and how the TV-TFM method captures the structures induced in M_t.

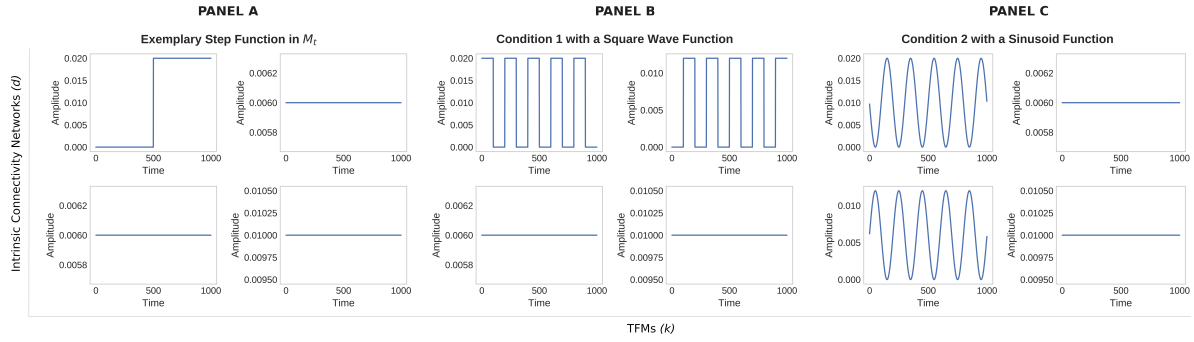

Figure 4. Induced structures in M_t: in panel A, a step function in entry $M_{t0,0}$ representing recruitment of an RSN by a certain TFM; in panel B, opposite square wave functions in entries $M_{t0,0}$ and $M_{t0,1}$, representing alternative recruitment of a RSN by two TFMs; in panel C, opposite sinusoid functions in entries $M_{t0,1}$ and $M_{t1,0}$, representing recruitment of two resting-state networks with opposite behavior by one TFM. Note, that these are examples: all structures were induced in a full-factorial manner.

2.2.2 Task-based fMRI.

Data were collected at the Robarts Research Institute at the University of Western Ontario in Canada. Healthy volunteers were recruited according to the guidelines of the Health Sciences Research Ethics Board of Western University. All volunteers provided written informed consent. Data were organised according to the Brain Imaging Data Structure (BIDS; Gorgolewski et al., 2016).

2.2.2.1 Sample.

Seventeen healthy volunteers participated in this study. Inclusion criteria were right-handedness and age below fifty years old. Visual inspection of data quality resulted in

the exclusion of three participants due to an acquisition error, i.e. the scanner timing was not well-matched to the presentation of stimuli. This resulted in a final sample of 14 participants between 19 and 32 years old, of which 7 were female (age: $M = 23.43$, $SD = 3.36$) and 7 were male (age: $M = 24.57$, $SD = 4.28$). For two of the participants, one individual run was excluded from the analysis, based on insufficient brain coverage.

2.2.2.2 Procedure.

Participants underwent one scanning session of about 40 minutes. It consisted of three runs of a visuomotor association task while functional magnetic imaging data were acquired, and an anatomical scan at the end of the task-run. Participants were trained on the visuomotor association task by performing one run before the scanning session. As visually presented in Figure 5, the task consisted of learning arbitrary associations between eight Japanese Kanji characters and four different motor responses, which were learned by trial and error. Between 25 and 36 ($M = 31.14$, $SD = 1.68$) visual stimuli were presented for 200ms. Participants were required to respond as soon as possible, but at least within 1.5s after stimulus onset. Motor responses consisted of pressing one of four buttons on a fibre optic response pad, where each button corresponded to two different Kanji characters. The response pad was placed on the abdomen of the participant, who consistently kept the index, middle, ring, and little fingers of the right hand on corresponding buttons. Performance feedback was given immediately after the response using three different sounds indicating a correct, incorrect, or too late response, respectively. Feedback was presented for 50 milliseconds, after which a fixation cross appeared until the next trial. Long inter-stimulus intervals (ISI) ranging between 16.19 and 41.59 seconds (one outlier of 80.47 sec; $M = 19.46$, $SD = 3.28$) were used, to ensure that the hemodynamic response would return to baseline before the next trial. Presentation of visual stimuli and registering motor responses was done using Presentation 20.1 (Neurobehavioral Systems, San Francisco, CA).

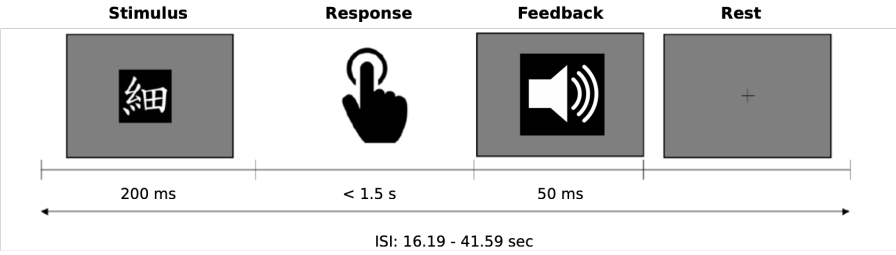

Figure 5. Schematic overview of the visuomotor association task.

2.2.2.3 Data acquisition.

Data were acquired on a Siemens MAGNETOM 7T MR scanner, equipped with a 32-channel head coil. The use of a highly optimized AC84 (GenII) head gradient engine with a maximum gradient strength of 80 mT/m and 2nd, 3rd, and 4th order shims, allowed the acquisition of T2* images at a very high temporal resolution. Functional images were acquired using a 2D multiband gradient-echo EPI protocol with an interleaved slice acquisition sequence (TR = 206 ms, TE = 22 ms, voxel sizes = 2.70 x 2.70 x 3.11 mm, flip angle = 20°, matrix size = 86 x 86, 32 slices, slice thickness/gap = 2.7 mm/3.1 mm, acceleration factor = 8). A

total of 3000 volumes were obtained per task-run of about 10 minutes, amounting to a total of 9000 task-based volumes across task-runs, per participant. Image reconstruction was performed using Slice-GRAPPA (Cauley et al., 2014; Hoge et al., 2018; Setsompop et al., 2012). For registration purposes, anatomical images were acquired using the MP2RAGE sequence (Marques et al., 2010; TR = 6s, TE = 2.3ms, voxel sizes = 1 mm isotropic, flip angles= 4 and 5 degrees; TI1 = 0.8s, TI2 = 2.7s; matrix = 240 x 240; 240 slices of 1 mm slice thickness).

2.2.2.4 Data pre-processing.

Data were pre-processed using fMRIPREP version 1.1.6 (Esteban et al., 2019), which is a Nipype-based tool (version 1.1.2; Gorgolewski, et al. 2011; Gorgolewski et al., 2018). Anatomical scans were corrected for spatial intensity variations using N4BiasFieldCorrection (ANTs 2.2.0; Tustison et al., 2010). A T1-weighted reference map was computed after registering the T1-weighted images using the mri_robust_template (Freesurfer, 6.0.0; Reuter et al., 2010). The T1-weighted reference was brain extracted using antsBrainExtraction.sh (ANTs 2.2.0) with a target template from the Open Access Series of Imaging Studies. Nonlinear registration to the ICBM 152 Nonlinear Asymmetrical template version 2009c (Fonov et al., 2009) was performed using antsRegistration (ANTs 2.2.0; Avants et al., 2008). The pre-processed T1-weighted reference map was used as a reference for functional registration. Brain tissue segmentation of the T1-weighted image into cerebrospinal fluid (CSF), white matter (WM), and grey matter (GM) was performed on the brain-extracted T1w using FAST (FSL v.6.0.0; Zhang et al., Jan./2001).

For all three task-based fMRI runs per participant, the following pre-processing steps were taken. Motion correction parameters were calculated using MCFLIRT (FSL 6.0.0, Jenkinson et al. 2002). A reference volume and its brain extracted version were generated using a custom methodology of fMRIPREP, i.e. averaging non-steady state volumes and computing a brain mask with init_enhance_and_skullstrip_bold_wf. Susceptibility distortions were estimated using a field map-less approach, i.e., registering the functional reference image to the T1w reference using intensity inversion (Huntenberg, 2014; Wang et al., 2017) while regularising by constraining deformation to be nonzero only along the phase-encoding direction and modulation with an average field map template (Treiber et al., 2016) as implemented in ANTs 2.2.0. The transformation parameters for co-registration to the T1w reference were calculated with MCFLIRT (FSL 6.0.0, Jenkinson et al., 2002), using boundary-based registration (Greve and Fischl, 2009) with 9 degrees of freedom. A concatenated transform to correct for head-motion, susceptibility distortion, functional to T1w registration, and registration from T1w to MNI space (i.e., MNI152NLin2009cAsym) was applied in one step using Lanczos interpolation (Lanczos, 1964), as implemented in antsApplyTransforms. Following Gomez et al. (2020) several confounding time series were computed, which were not used to denoise the functional time series but to measure whether they correlate to the TFM time series. This concerned: three region-wise global signals, extracted within the CSF, the WM, and the whole-brain mask. The head-motion estimates from MCFLIRT were also placed within the corresponding confounds file. Datasets were temporally high-pass filtered with a cut-off frequency of 0.01 Hz (i.e., a periodicity of 100s)

and spatially smoothed with a FWHM of 5.4mm. ICA-based denoising of the data was performed. Each pre-processed run was decomposed into 70 spatial independent components using Probabilistic Independent Component Analysis (Beckmann and Smith, 2004) as implemented in MELODIC (version 3.15, FSL). The following data pre-processing was applied to the input data: masking of non-brain voxels, voxel-wise de-meaning of the data, normalisation of the voxel-wise variance, and subsequent whitening and projection into a 70-dimensional subspace using Principal Component Analysis. The whitened observations were decomposed using spatial ICA (Hyvarinen, 1999). Estimated component maps were divided by the standard deviation of the residual noise and thresholded by fitting a mixture model to the histogram of intensity values (Beckmann and Smith, 2004). IC components were manually classified into signal and noise and the pre-processed data were de-noised using FSL REGFILT (FSL v.6.0.0, Jenkinson et al., 2012). The pre-processed data were moreover variance normalized (mean zero and unit standard deviation across time) using FSLMATHs (FSL v.6.0.0, Jenkinson et al., 2012).

2.2.3 Statistics.

For the proof of concept using the task-based fMRI dataset, explorative statistical analyses were conducted at the single task-run, single-subject– and at the group level. The well-established dual-regression technique (stage 1), the classical time-averaged TFM model (stage 2) and the new TV-TFM model (new stage 3) were exploratively compared in their ability to capture task-based variation in high temporal resolution FMRI data of participants performing a visuomotor association task. Single-subject results are illustratively presented for one task-run, of one participant (subsequently referred to as *'the selected dataset'*). Criteria for selecting this dataset for illustrative purposes are outlined in section II of the Supplementary Material.

First, it was examined how well task-related variability is captured: i) in the dual-regression time series; ii) in the TFM time series as obtained with classical TFM analysis, and iii) in the time-resolved mapping of TFMs onto the resting-state networks as obtained with TV-TFM analysis. Therefore, at each stage of the analysis pipeline (dual-regression, classical TFM analysis, and TV-TFM analysis) a first-level analysis was run separately for each task run, consisting of pairwise Pearson correlations between the time series and the task regressors of the visuomotor association task (i.e. visual stimulation and motor response).

To account for dependencies between task-runs per participant, for stage one (dual-regression) a fixed-effects analysis was run on the Fisher-Z transformed correlation values of the association between the dual-regression time series and the task regressors. That is, they were averaged over task-runs, per participant. To identify the resting-state network time series that across participants were significantly related to the task, a third-level analysis was performed using a one-sample t-test per network.

At stage two of the analysis pipeline (classical TFM analysis), group-level comparisons per TFM are problematic due to the correspondence problem of temporal ICA. It was therefore examined whether per task-run TFM time series (i.e. B) better capture task-related variability than dual-regression time series (i.e. T). This was done by first selecting the dual-regression time series and the TFM time series that showed the strongest absolute

correlation to the visual task regressor. The Fisher-Z transforms of these absolute correlation values were then compared per task-run using a paired sample t-test.

For the new third stage of the analysis pipeline (TV-TFM analysis), it was first examined whether f predicts task-related variability over and above the TFM time series from stage two (classical TFM analysis). This was done for the selected dataset using two hierarchical analyses, separately predicting the visual and the motor task regressor. For both analyses, the time series of the TFM that was most strongly associated with the visual task regressor was entered in step one, and the entries of f related to that TFM were entered in the second step.

The DMN is widely recognized as a task-negative network (Singh and Fawcett, 2008). We therefore tested whether we observed an unfolding, increasing difference between the DMN and task-positive network (i.e. visual, sensorimotor and auditory) weights in entries of the time-varying mixing matrix, for task-relevant TFMs. This was done using an event-related approach. It was first examined whether this pattern was observed across trials. Therefore, per task-run, entries of f that corresponded to the TFM that showed the strongest absolute correlation with the visual task regressor were averaged across trials. A trial consisted of a 60-frame epoch (i.e. $60 \times 0.206ms = 12.36$ seconds), starting at the onset of the visual stimulus. This interval was chosen such that it covers most of the expected time it takes for the hemodynamic response to increase in response to the visual stimulus and planning a motor response as well as come back to baseline, while not overlapping between trials. Note that if the strongest correlation was negative, the direction of the time series was reversed because it is not informative (i.e. it depends on the sign of the mixing matrix weight). Differences between the trial-averaged DMN weight and each of the three trial-averaged task-positive network weights (i.e. the average of the primary and lateral visual weights, the sensorimotor weight and the auditory weight) were then separately tested per time frame using a paired t-test. To account for dependencies between task-runs per participant, a fixed-effects analysis was run. That is, the t-values were averaged across task-runs, per participant. Lastly, it was examined whether an increasing difference between the DMN weight and each of the task-positive network weights in response to the task was observed across participants. This was done by computing a group-level Z-value per time point, for the comparison between the DMN and each of the task-positive networks, separately.

3 Results

3.1 Synthetic data

Simulations were performed to explore the properties of the new TV-TFM model. They were performed with different parameters to construct B, and with different signal-to-noise-ratios. Given the exploratory nature, merely one set of results are presented for illustrative purposes in Figure 6. These simulations were performed with the following parameters for the construction of B: $loc_1 = 2.0$, $scale_1 = 5.0$ for the first time series and $loc_1 = 3.6$, $scale_1 = 4.4$ for the second time series. The product of the simulated M_t (as presented in panel A of the figure) and B, provided the data X to which a random noise factor ($\mu_X = 0$, $\sigma_X = .001$) was added. Panel B shows the time series retrieved with temporal ICA,

and panel C shows the time-varying mixing matrix retrieved with TV-TFM analysis. In the first row, panel C, we observe that the structure of the independent ICA time series is present in all entries of the associated column of $\hat{M}_t$. This is unsurprising given that $\hat{M}_t$ consists of the element-wise product between X and $\hat{B}^\intercal$ (scaled by the co-variance of B). The patterns observed in M_t after inducting an anti-correlated pattern in the "TFM" entries (second row) and in the "resting-state network" entries (third row) are hard to interpret. Nevertheless, the simulations guided further development steps. For example, the decision to work with f, such that variability around the time-averaged M is probed (whereas M_t *sums* to M).

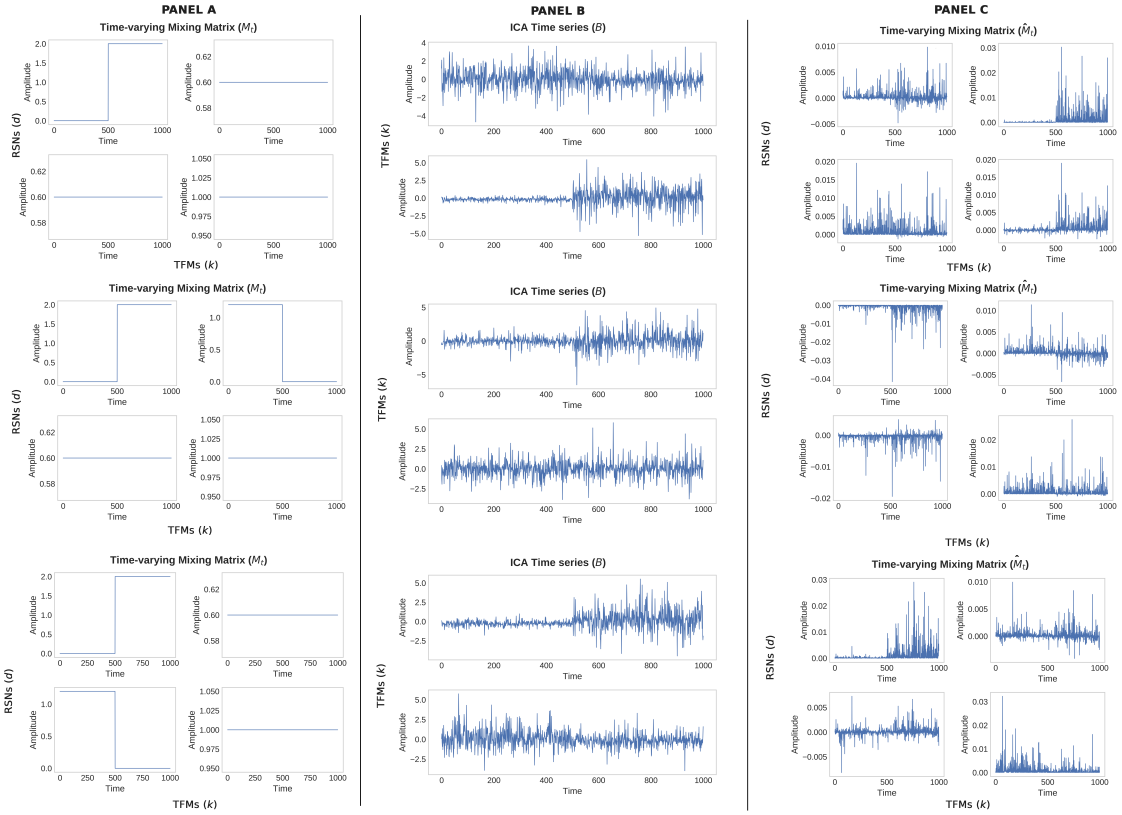

Figure 6. Illustrative results of one set of simulations. Panel A shows the structure induced in M_t. Panel B visually presents the independent time series extracted with temporal ICA. Panel C shows the time-varying mixing matrix extracted with TV-TFM analysis.

3.2 Task-based fMRI

3.2.1 Stage 1: Canonical resting-state networks.

Dual-regression with respect to the brain network templates by Smith et al. (2009), resulted in a set of canonical resting-state networks per task-run, per subject, and per spatial network template (SMITH20 and SMITH70 templates). As previously described, the results described stem from a spatial decomposition by means of dual-regression against the SMITH20 template. The resulting resting-state networks are described by a spatial map (see, e.g., Figure 7) and a corresponding time series (see, e.g., the right side of Figure 8).

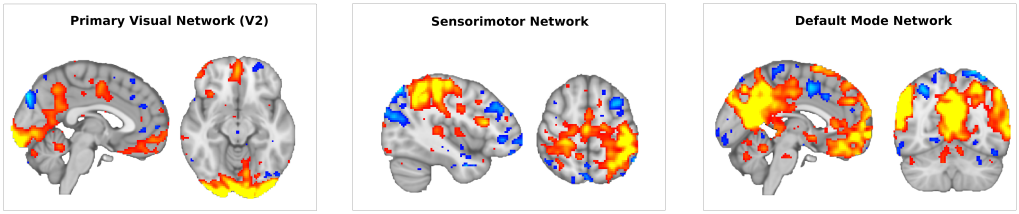

Figure 7. Two representative slices of the dual-regression spatial maps of the primary visual network (visual 2 of the SMITH20), the sensorimotor network and the default mode network, for the selected dataset (thresholded at $Z > 5$).

Bonferroni corrected, Pairwise Pearson correlations between the dual-regression time series and the visuomotor association task regressors (i.e. visual stimulation and motor response) are illustratively presented for the selected dataset in Figure 8.

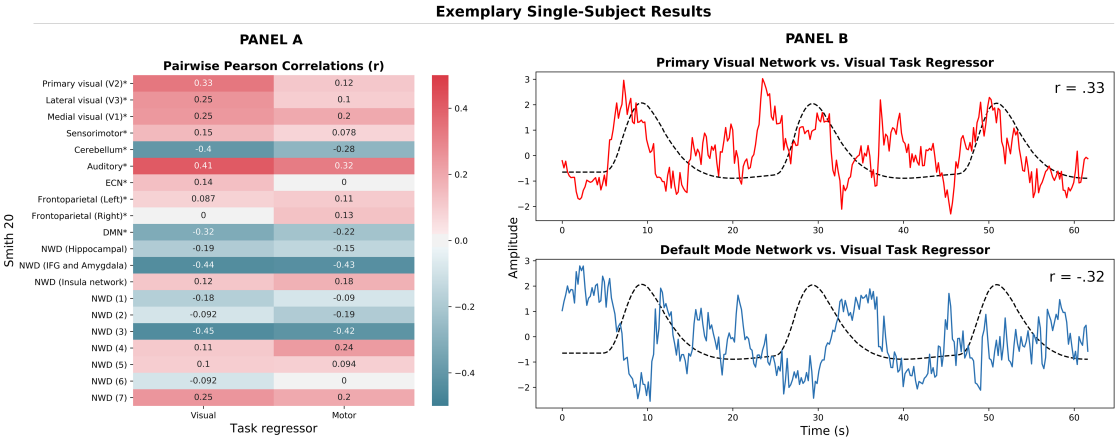

Figure 8. Panel A shows Bonferroni corrected (i.e. significance below .05/20 = .0025; *ns.* correlations set to zero) pairwise Pearson correlations between the dual-regression time series and the visual and motor task regressor, for the selected dataset. Panel B shows a sample of the dual-regression time series for the primary visual network and the DMN plotted against the visual task regressor. Note that the DMN is generally considered to be a *task-negative* network (Singh and Fawcett, 2008), based on which the observed anti-correlated pattern is in line with the expectation.

Whether the *group* averages of the Fisher-Z transformed correlation values were significantly different from zero was tested for each network with a one-sample t-test. Bonferroni corrected results are presented in Figure 9.

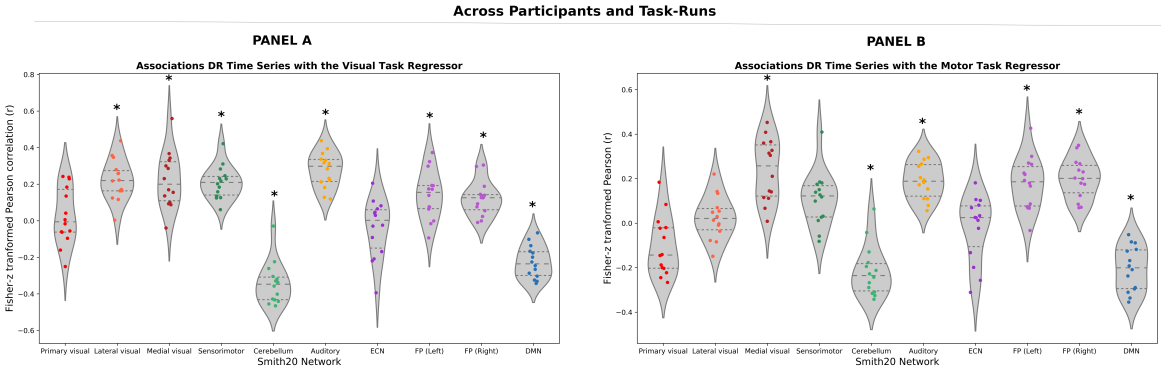

Figure 9. Distributions of correlation values between the DR time series of the ten well-defined networks as obtained by Smith et al. (2009) and the visual task regressor (panel A) and motor task regressor (panel B). Note: (*) Significantly different from zero as assessed by one-sample t-tests, Bonferroni corrected (i.e. significance below .05/20 = .0025); abbreviations: ECN = executive control network, FP = frontoparietal network, DMN = default mode network.

The following findings are relevant for the purpose of the present paper. As visually represented in Figure 9, across participants *correlations with the task regressors were found across most of the networks*. This indicates that task-related information is distributed across the dual-regression time series of the different resting-state networks. Note that contrary to the expectation, the primary visual network (V2) did not significantly relate to the onsets of the visual stimulus, Fisher-$Z = 0.03$, $t(13) = 0.63$, $p = .537$, nor did the sensorimotor network significantly relate to the motor responses, Fisher-$Z = .11$, $t(13) = 3.30$, p = .006 (after Bonferoni correction; i.e. significance below $.05/20 = .0025$). Please refer to the Supplementary Material, section III for an overview of the statistics of all one-sample t-tests.

3.2.2 Stage 2: Temporal functional modes.

Temporal ICA resulted in a set of TFMs per task-run, per subject, per spatial network template (SMITH20 and 70) and per temporal ICA dimensionality (8, 10, 15, and 21 depending on the model order of the spatial template). As previously addressed, the results described stem from the highest model order, i.e. 15, for the SMITH20 template. TFMs are described in terms of their weighting onto the SMITH templates (node weights/a mixing matrix column, see e.g. Figure 10) and the corresponding time series. TFM time series were related to confound regressors, as an indication of their neuronal basis. Results are presented in section IV of the Supplementary Material.

As visually illustrated for the selected dataset in Figure 10, we identified a "task-positive mode" which includes regions related to the visual, motor and auditory aspects of the task, i.e. primary visual (occipital pole), medial visual (e.g. lingual and occipital fusiform gyri) and lateral occipital regions; the temporal pole; motor regions along the dorsal stream (e.g., primary motor cortex and supplementary motor cortex) and primary auditory cortex. A similar component was identified across most task-runs and participants. Please refer to section V of the Supplementary Material for further details.

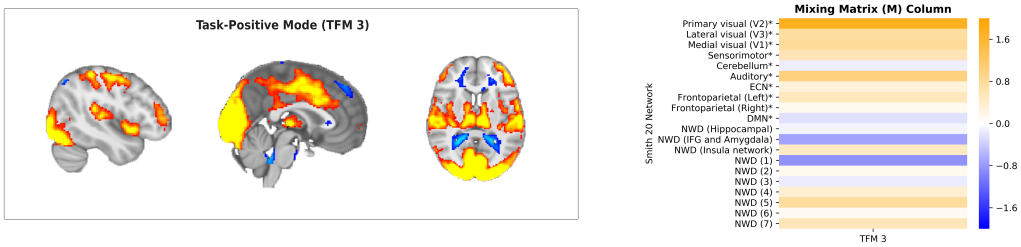

Figure 10. Three representative slices of the task-positive mode, i.e. the TFM that correlated most strongly to the visual task regressor for the selected dataset (thresholded at $Z > 5$), and the associated mixing matrix column.

We moreover identified a similar component to the most common TFM identified by Gomez et al. (2020), the "default temporal mode", consisting of core hubs of the DMN (i.e. angular gyrus and precuneus) in anti-correlation with the motor regions (superior parietal cortex, post-central gyrus and supplementary motor cortex), the auditory network, and the insula (see Figure 11). A similar component was identified across most task-runs and participants. Please refer to section V of the Supplementary Material for further details. Note that contrary to the findings by Gomez et al. (2020) no anti-correlations with visual areas were found for the selected dataset. This potentially results from component splitting, since a

temporal ICA of model-order ten performed on the time series of the ten well-defined networks of the SMITH20 template, identified a component similar to the default temporal mode *also in anti-correlation to visual areas* (see the Supplementary Material section VI).

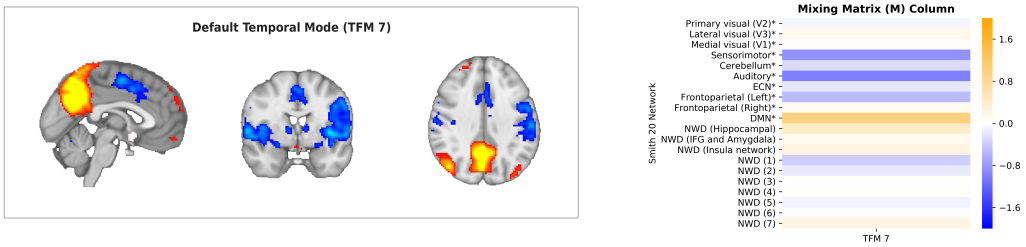

Figure 11. Three representative slices of the default temporal mode (TFM7; thresholded at $Z > 5$), and the associated mixing matrix column.

Bonferroni corrected, Pairwise Pearson correlations between the TFM time series and the visuomotor association task regressors are illustratively presented for the selected dataset in Figure 12. The previously described "task-positive mode" (TFM3) correlated most strongly with the visual task regressor. TFM14 correlated most strongly with the motor task regressor.

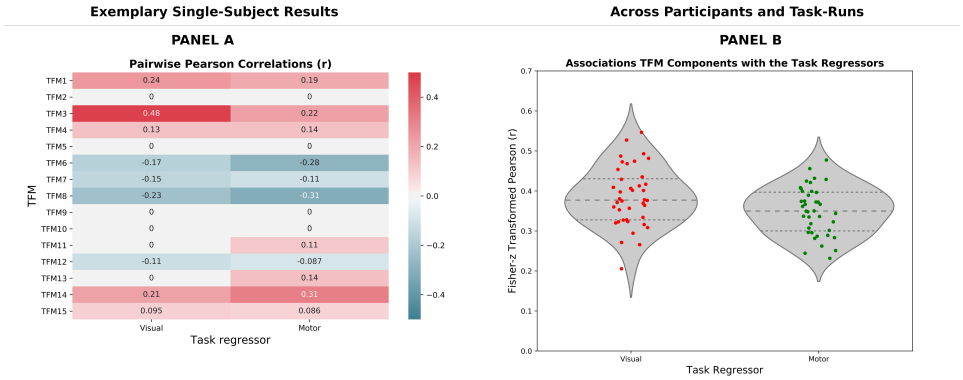

Figure 12. Panel A shows Bonferroni corrected (i.e. significance below .05/15 = .003; *ns.* correlations set to zero) pairwise Pearson correlations between the TFM time series and the visual and motor task regressor illustratively for the selected dataset. Panel B shows the distributions of correlation values for the TFMs most strongly associated with the visual and motor task regressor, across task-runs and participants.

A visual representation of the spatial map of TFM14 is presented in Figure 13. It consists of an anti-correlated pattern between the frontoparietal attention network and the temporal fusiform cortex, a higher-level visual processing area involved in sensory integration and memory.

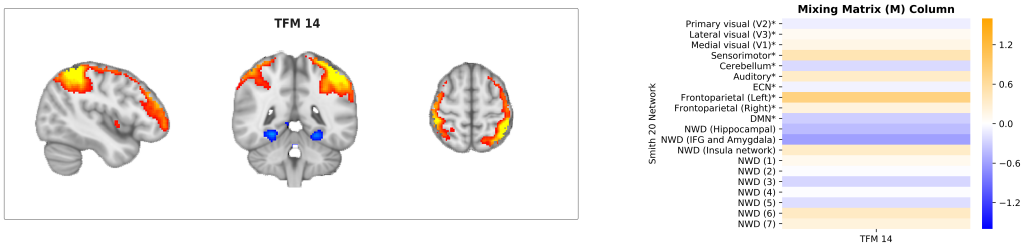

Figure 13. Three representative slices of the TFM spatial map that correlated most strongly to the motor task regressor for the selected dataset (thresholded at $Z > 5$), and the associated mixing matrix column.

In panel B of Figure 12, correlation values are plotted for the TFMs that correlated most strongly with the visual (left) and motor (right) task-regressor, per task-run. A relevant observation for the purpose of the present paper is the *increased sparseness of the correlation matrix*, as observed in panel A of Figure 12, compared to the dual-regression correlation matrix in Figure 8. That is, task-related variation appears to be represented in fewer components. This corresponds to the fact that temporal ICA retrieves temporally independent processes, consisting of linear combinations of resting-state networks. Moreover, it was found that across task-runs, absolute correlations with the visual task regressor were stronger for TFMs (which per task-run correlated most strongly to the task), than for dual-regression time series (which per task-run correlated most strongly to the task), *paired-t*$(39) = 5.05$, $p < .0001$. This is in line with the conceptual expectation that –at least for some participants and to some extent– task-related processes are temporally independent from other brain processes, and can be captured using temporal ICA.

3.2.3 New stage: Time-varying temporal functional modes.

TV-TFM analysis resulted in time-varying mixing matrices (i.e. M_t and its scaled version f) per: i) task-run, ii) participant, iii) spatial network template (SMITH 20 and 70), and: iv) temporal ICA dimensionality (8, 10, 15, and 21 depending on the spatial model order). As previously described, the results described stem from the highest model order, i.e. 15, for the better defined SMITH20 template.

TV-TFMs can be described spatially by means of the product between the spatial maps, S, and the entries of the time-varying mixing matrix related to one TFM component. This allows per time point visualizations of the resting-state networks (as identified by Smith et al. (2009)) recruited by this TFM. An example for the selected dataset is presented in Figure 14, where the temporal evolvement of the task-positive mode (TFM3) is presented for one trial. Onsets of the visual stimulus and motor response as presented on the bottom of the Figure, and are operationalized as the first time frame that the stimulus/response convolved with the HRF exceeds zero. Time-locked to the visual stimulus we observe recruitment of primary visual areas, followed by medial and lateral visual areas. Time-locked to the motor response we observe the recruitment of superior parietal motor regions, and subsequent recruitment of the pre-central gyrus/primary motor cortex.

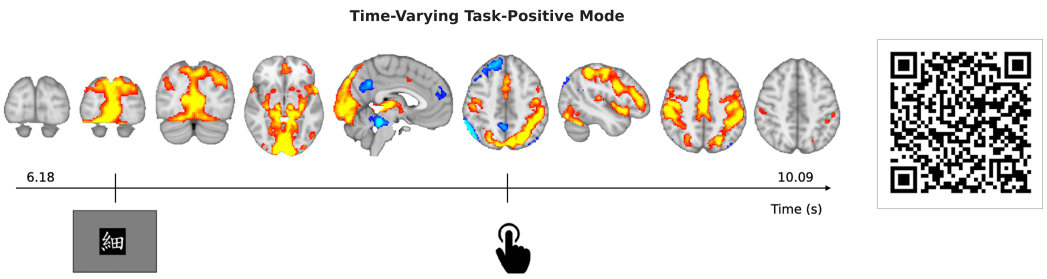

Figure 14. Representative slices of the time-varying task-positive mode (TFM3) for the selected dataset. The onsets of the visual stimulus and the motor response, as visually presented on the bottom of the figure, are defined as the first time frame that the stimulus/response convolved with the HRF exceeds 0. On the right a QR that links to a video of the entire trial (from two frames before the onset of the visual stimulus until 8 frames after onset of the motor response).

Figure 15 presents a sample of the time series of the time-varying mixing matrix (f) illustratively for the selected dataset. In panel A entries of the task-positive mode (TFM3) for task-relevant networks are plotted for the duration of two trials for the selected dataset. Entries of f closely follow the expectation based on the task design for the first trial, recruiting the primary visual network, the sensorimotor network and the auditory network subsequently. Additionally evident from this figure is the high-frequency content that is characteristic of f. Ranking-ordering the entries of f per TFM, per time-point, for example, allows to examine (in a crude manner) which networks are most strongly recruited by the respective TFM over time. An example for the task-positive mode (TFM3) is presented in panel B of Figure 15, for the selected dataset. The bottom plot in panel B shows per network when in time its weighting was the strongest (i.e. it had the highest rank) for two trials. The top plot in panel B shows the highest-ranking network per time point, plotted on the visual task regressor for these same two trials. We observe that for the first trial the ranks closely follow the expectation based on the task design, such that in response to the onset of the visual stimulus the visual networks predominate, followed by short periods in which the sensorimotor network and the auditory network subsequently rank highest. Both before the onset of the stimulus and after the stimulus, the default mode network ranks highest. This pattern is less clear in the second trial.

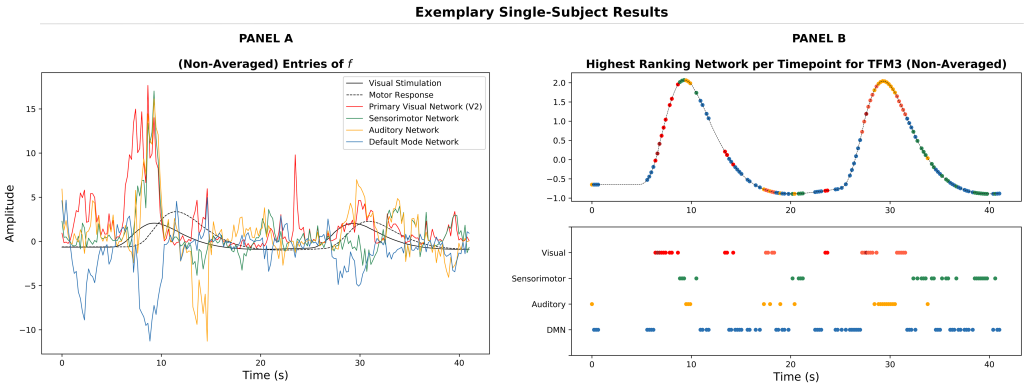

Figure 15. In panel A, raw entries of f for TFM3 and task-relevant networks are plotted for two trials, for the selected dataset. In panel B the highest-ranking network is plotted on the visual task regressor for TFM3.

Pairwise Pearson correlations between each entry of f and the visuomotor association task regressors are illustratively presented for the selected dataset in Figure 16. The sum of the correlation values across the entries of each TFM was highest for TFM3 for the visual task regressor, and for TFM14 for the motor task regressor (see Supplementary Material, section VII). These are the same TFMs for which the time series were most strongly related to the task regressors (as concluded in stage two of the analysis pipeline; see Figure 12). In line with the expectation, correlations between the visual task regressor and the TFM3 entries that correspond to the task-positive networks (i.e. primary and lateral visual, sensorimotor and auditory) are opposite to the correlation between the visual task regressor and the TFM3 entry that corresponds to the DMN. This pattern is slightly different for the correlations between the motor task regressor and the entries of TFM14, in the sense that no significant correlations with the lateral visual network (V3) and the DMN were found.

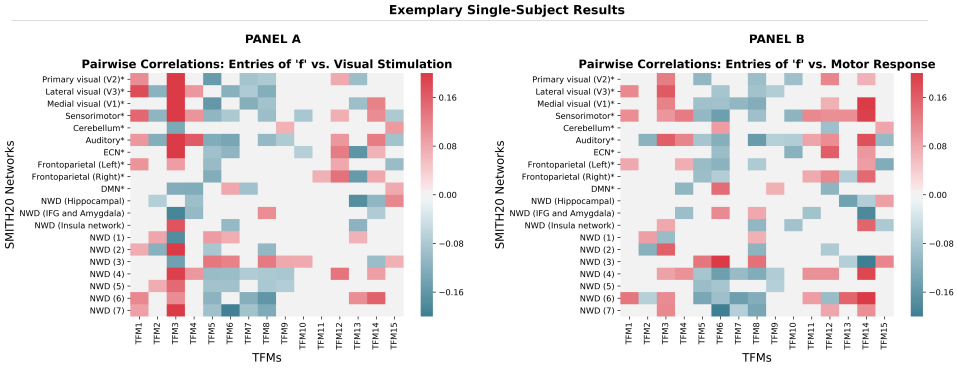

Figure 16. Bonferroni corrected (i.e. significance below .05/300 = .0002; *ns.* correlations set to zero) pairwise Pearson correlations between the entries of f and the visual and motor task regressor, in panel A and B respectively, illustratively for the selected dataset.

For the hierarchical regression analysis predicting the visual task regressor, the time series of TFM3 explained 23.3% of variance, $F(1, 2999) = 913.5$, $p < .0001$. Adding the entries of f relating to TFM3, explained an additional 5.0 % of variance, a significant change in the adjusted R^2, $F(15, 2984) = 14.92$, $p < .0001$. For the analysis predicting the motor task regressor, the time series of TFM14 explained 9.7% of variance $F(1, 2999) = 323.20$, $p < .0001$. Adding the entries of f relating to TFM14 explained an additional 7 % of variance, a significant change in the adjusted R^2, $F(15, 2984) = 17.73$, $p < .0001$.

The event-related approach, consisting of trial-averaging f, provided the main proof-of-concept for TV-TFM analysis. Trial-averaged entries of f for TFM3 and the task-relevant networks are presented for the selected dataset in panel A of Figure 17. We observed that the TFM3 entries of f closely followed the task-design, i.e. starting with an increase in the primary visual network, followed by increases in the sensorimotor network and the auditory network, and a concurrent decrease in the DMN weights. A similar but smaller effect, time-locked to the motor regressor, was found for TFM14 (of which the time series were most strongly related to the motor task regressor; see panel B). For comparison, in panel C an example is plotted for a TFM for which the time series were not significantly related to the task.

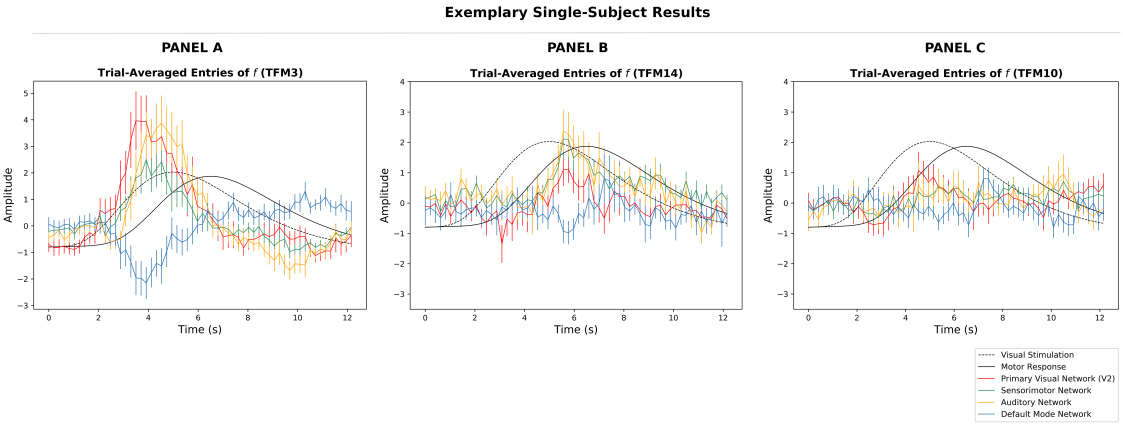

Figure 17. Trial-averaged entries of f for the task-relevant networks, for TFM3 in panel A, for TFM14 in panel B and for a TFM unrelated to either regressor in panel C (for the selected dataset). Note that the error bars represent the standard error of the mean.

A similar pattern was found across most task-runs and participants. Please refer to section VIII of the Supplementary Material for trial-averaged plots of task-relevant entries of f per task-run, per participant. Support for the observed trend was obtained by means of per time frame paired t-tests on the *differences between the DMN and each task-relevant entry of f separately*, for the trial-averaged f. That is, DMN versus the average of the primary and lateral visual weights, DMN versus the sensorimotor weight and DMN versus the auditory weight. Group level results (after averaging across task-runs per participant at the second level) for the TFMs which showed the strongest absolute correlation with the visual and motor task regressor are presented in panel A and B of Figure 18, respectively. In both cases, across trials, task-runs and participants, the differences between the DMN and: i) the average of the primary and lateral visual entries, 2) the sensorimotor entry, and 3) the auditory entry increased subsequently.

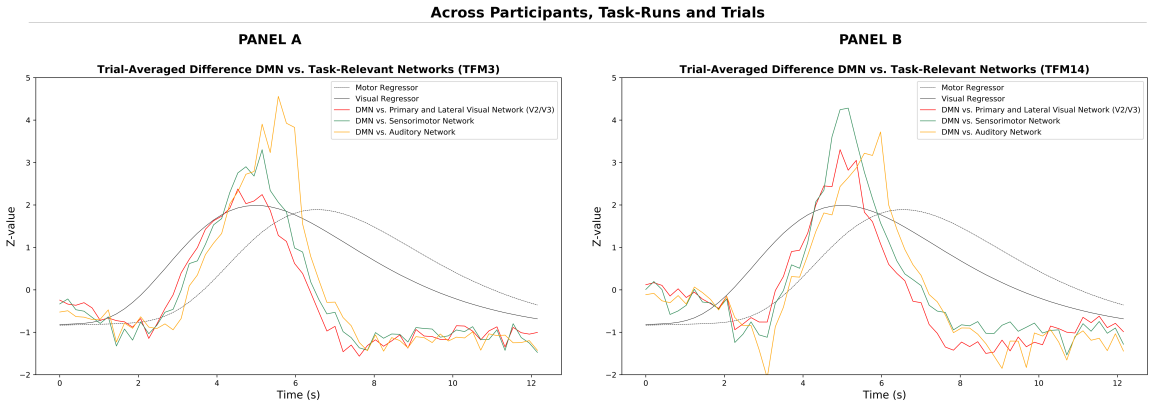

Figure 18. The Z-distributions of the differences between the DMN and the: i) average of the primary and lateral visual network; ii) the sensorimotor network and iii) the auditory network, across trials, task-runs and participants. Presented for the TFMs that correlated most strongly to the visual task regressor in panel A, and for the TFMs that correlated most strongly to the motor task regressor in panel B.

As a first parametrization, the Z-distributions of both TFM3 and TFM14 presented in Figure 18 were fitted with three independent gamma distributions, with:

$$\gamma = \frac{\beta^{\alpha}}{\Gamma(\alpha)} x^{\alpha-1} \exp^{-\beta x} \tag{14}$$

The model fitting was performed after restricting the time-range, shifting the distributions up into the positive domain of Z and normalizing the distributions (such that they integrate to one). The parameters for these operations are presented on the left side of Table 1. The parameters for the best fitting gamma distributions and the sum of squared errors (SSE) are presented on the right side of Table 1. Based on these distributional parameters we can indeed disentangle the visual, sensorimotor and auditory distributions for TFM3 (of the differences with the DMN; for a visual representation see Figure 19).

Table 1
Parameters for Model Fitting of Gamma Distributions.

	Operation Parameters: time range (s)	shift in y
TFM3		
Visual	1.44 - 12.36	1.15
Sensorimotor	1.44 - 12.36	1.03
Auditory	1.44 - 12.36	0.88
TFM14		
Visual	2.27 - 12.36	0.94
Sensorimotor	2.27 - 12.36	1.24
Auditory	2.27 - 12.36	0.65

	Model Fit Parameters: α	β	Mode (s)	SSE:
TFM3				
Visual	8.54	0.51	3.05	5.71
Sensorimotor	12.47	0.72	3.28	5.90
Auditory	23.45	1.21	3.82	30.46
TFM14				
Visual	10.51	0.75	2.61	6.26
Sensorimotor	7.88	0.51	2.78	6.77
Auditory	23.12	1.41	3.23	17.82

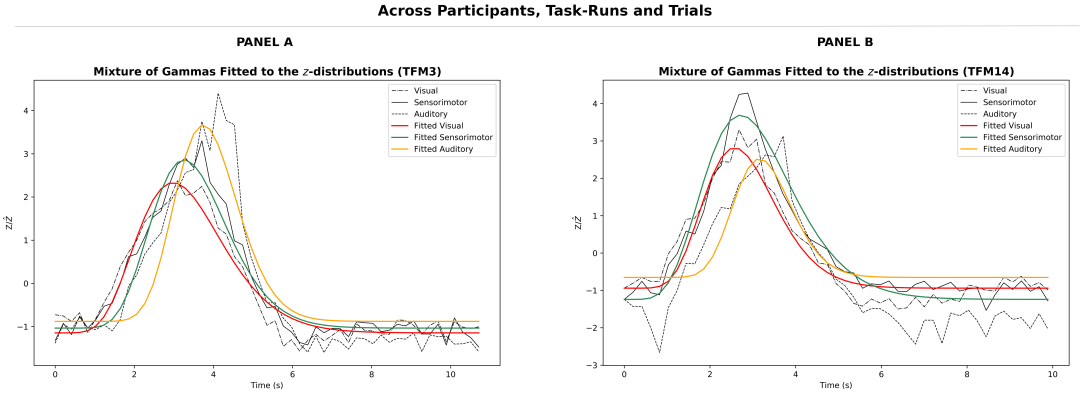

Figure 19. The Z-distributions of the differences between the DMN and the: i) average of the primary and lateral visual network; ii) the sensorimotor network and iii) the auditory network, across trials, task-runs and participants, fitted with three Gaussian distributions. Presented for the TFMs that correlated most strongly to the visual task regressor in panel A, and for the TFMs that correlated most strongly to the motor task regressor in panel B.

4 Discussion

4.1 Proof-of-Concept

With the current study, we provided the first proof-of-concept for TV-TFM analysis. The goal was to develop a time-varying method that allows for spatial overlap. The latter is inherently safeguarded by extending classical TFM analysis, which allows for spatial overlap by following a spatial decomposition with a subsequent temporal ICA on the retrieved time series. That the same spatial component can indeed be recruited by different temporal processes shows from the fact that different temporally independent processes (TFMs) map onto the same spatial maps. Regarding the first, TV-TFM analysis obtains moment-by-moment estimations of the extent to which different spatial components (e.g. resting-state networks) are recruited by certain temporally independent processes (TFMs). The main validation was provided by applying TV-TFM analysis to task-based fMRI data and subsequent event-related averaging of the time-varying mixing matrix entries per resting-state network, for the TFMs that correlated most strongly to the task. The pattern observed across participants, sessions, and trials, closely followed the expectation based on the task design, such that we observed an increase in visual areas, the sensorimotor network, and the auditory network, subsequently. Differences in timing between these subsequent increases were small.

This is inherent to the task design, in which the different processes follow each other up in close succession: the visual stimuli are presented for 200ms, participants are required to respond as soon as possible by means of a button press and get immediate auditory feedback. Previous attempts to temporally disentangle these processes in high-temporal resolution fMRI data by means of a mass univariate GLM approach correspondingly were unsuccessful (Noteboom, 2018). At the very fast TR of .206ms in the current study, we also could not disentangle the processes using dual-regression with respect to existing resting-state network templates. In part, these processes were also considered a joint independent temporal process as identified by temporal ICA. That is, applying temporal ICA at stage two of the analysis pipeline resulted in a task-positive component which included brain regions implied in all these processes (i.e. visual, motor and auditory). Albeit with small differences when averaged over trials, task-runs and participants, TV-TFM analysis proved to be a step forward towards temporally disentangling them. It should be noted that event-related averaging could also have been applied to T, i.e. the dual-regression time series. This would have provided a linear mix of resting-state networks at a full brain level. With the approach taken in the current study, however, we retrieved a linear mix of *temporally independent processes*. We argue that this is a reasonable approach because it aids interpretability by reducing the dimensionality to task-related information (i.e. a task-related temporally independent process).

4.2 Model Assumptions

The latter points to an important assumption of the model, namely that temporal ICA at stage two of the analysis adequately identifies the process of interest. Preliminary support for the idea that stage two of the analysis pipeline does indeed capture task-related variability was provided by Gomez et al. (2020), who concluded that TFM time series carry an imprint of the task design. Our present results provide some additional support. First, based on the observation that classical (time-averaged) TFM analysis increases specificity in detecting task-related variability compared to the dual-regression approach. That is, correlations of dual-regression time series with the task were widespread across networks, whereas correlations to the task were identified for a smaller number of TFMs. The TFM components that correlated most strongly to the task regressors, moreover spatially involved regions expected to be involved in the visuomotor association task. Studies probing the ability of temporal ICA, or classical TFM analysis specifically, to adequately capture task-related variability are however scarce and this hence requires further assessment. In this study, we used a simple, but effective approach to probe whether the identified temporally independent processes were task-related, i.e. temporal correlation. This was decided, in part, because of multicollinearity among the task regressors. For the same task paradigm, this was also found by Noteboom (2018), who suggested that this might be a primary reason that the GLM is unable to temporally disentangle these processes. For other task paradigms, we however suggest using regression analyses within a general linear model, which allows adjusting for covariates such as handedness (note that in the current study this specific example was addressed in the inclusion criteria). Other, more advanced, e.g. PCA-based, supervised approaches could also be explored.

4.3 Limitations and Future Directions

In the current study we obtained the instantaneous correlations between the individual spatial maps regressed onto the *noiseless reconstruction of the fMRI data*, and the TFM time series (scaled by their covariance) to retrieve moment-by-moment estimations of brain network reconfigurations. If a process of interest is not captured adequately using classical TFM analysis, the task-relevant information is unexplained, residual variance. In that case, it could well be that the reconfigurations are better characterised using the original, instead of the noiseless reconstruction of, fMRI data. That is, accounting for the residual errors should hence be considered in the future.

We believe that are several other future steps to be taken to further validate this method. First of all, the Z-values describing the differences between the network entries of f across trials, task-runs, and participants were not statistically tested for the current proof-of-concept. Note that doing so in the future, requires non-parametric, permutation testing since the averaging of t-values at the second level breaks the assumption of normality (i.e. it is t–, not normally, distributed). Improving the simulations could moreover potentially help to further validate the method. In a first attempt to probe properties of the new model, highly simplified scenarios were simulated in the current study. In the future, we aim to perform more biologically plausible simulations by modifying fMRI data.

We see several other potential courses of action to improve the TV-TFM method. It was observed that the time series of f are characterised by a large amount of high-frequency content. In the current proof-of-concept, this was dealt with by averaging over trials. In the future, we would however like to apply this method at the single-trial level. Whereas we parametrized the Z-distributions by fitting independent Gamma distributions, we aim to fit a mixture-model (potentially of another distribution, e.g. Inverse Gaussian) to the Z-distributions at the single-trial level in the future, followed by a PCA analysis. Herewith, differences in timing and/or shape of these distributions would potentially allow predicting behavioural measures such as success vs. unsuccessful trials or attentiveness or inattentiveness to the task. These parameters could also be related to state and trait measures, via which this approach could be applied in the clinical domain. Application at the single-trial, single-subject level however likely requires smoothing of f, for example by means of a Kalman filter.

Another important follow-up step is to develop a dual-regression-like approach to deal with the correspondence problem at stage two, temporal ICA, in order to probe and compare similar temporally independent processes of interest across participants. Although Gomez et al. (2020) found that similar TFM components are found independent of the initial spatial dimensionality reduction, we suggest that it might be relevant to explore the results of TV-TFM analysis after different initial spatial dimensionality reductions. First, the finer-grained SMITH70 template. The SMITH20 template used in the current study was obtained with a model-order that has proven to robustly identify the canonical large-scale resting-state networks in resting-state fMRI (Smith et al., 2009). A model-order of 20 was also shown to be optimal for decompositions of BrainMap-based ICA components. At higher granularities it was found that subnetworks at lower levels of the functional hierarchy are identified(Ray et al., 2013). This level of detail would be of interest especially studying

task-based fMRI data, given the idiosyncrasies of cognitive tasks. Brain network reconfigurations as obtained with TV-TFM analysis after anatomical (instead of functional) parcellations, could also be explored.

4.4 Potential applications

The developed model has numerous potential applications. For example, temporal ICA could be applied to an ROI, such that for a temporal process of interest, f describes how sub parcels interact over time. Instead of following the spatial and temporal decomposition in TFM analysis, the time-varying approach proposed in the current study could also be implemented for other initial spatial parcellations and other subsequent multivariate dimensionality reduction methods. For the latter, a supervised PCA-based multivariate method like SPADE (Llera et al., 2020) would be an option, were moment-by-moment estimations are obtained for so-called filters which optimally discriminate between certain conditions. Irrespective of the application, the goal is eventually to utilize the information present in the time-varying matrix. For example, by describing the timing and/or shape differences of the Z-distributions in different states or conditions and between different individuals, where these parameters describe inter-individual differences in brain network reconfigurations (while allowing for spatial overlap).

4.5 Contribution

We believe TVTFM analysis makes a relevant contribution to the current landscape of TVFC methods. First, because it leverages a new feature to probe TVFC, namely *a time-varying mixing matrix*. Secondly, because of its high temporal resolution. As previously described, the current TVFC methods can be differentiated based on the time-window they consider, ranging from instantaneous measures to time windows of 30-60 seconds common in sliding-window analyses (Preti et al., 2017). TV-TFM analysis provides moment-by-moment, or per timeframe, estimations of TVFC. Thirdly, it has been addressed that several dimensionality reductions are generally performed in TVFC analysis. Instead of ignoring temporal ordering of the data, as is done in several TVFC methods by means of k-means clustering for example, the dimensionality reduction consists of zooming in on one or more temporally independent processes of interest which are derived in a data-driven manner (by means of temporal ICA). Although it could be argued that the complexity of the present method is relatively high (i.e. with respect to the number of analysis steps, and the mathematical derivation), we believe that interpretability is a strong point because the estimated brain network reconfigurations are described in space and time for certain processes of interests. Identification of the process of interest for the task-based fMRI dataset was done in the present study by correlation to the task regressors. Identification of a process of interest could also be done in a different manner, for example based on physiological arousal measures, which would allow extending this method to resting-state fMRI. To conclude, we hope that in the future this new method will further elucidate the temporal properties of functional brain networks and that it will have a significant clinical contribution, e.g. by probing temporal differences in brain network reconfigurations between individuals.

5 References

B. Avants, C. Epstein, M. Grossman, and J. Gee. Symmetric diffeomorphic image registration with cross-correlation: Evaluating automated labeling of elderly and neurodegenerative brain. *Medical Image Analysis*, 12(1):26–41, Feb. 2008. ISSN 13618415. doi: 10.1016/j.media.2007.06.004.

P. A. Bandettini. What's New in Neuroimaging Methods? *Annals of the New York Academy of Sciences*, 1156(1):260–293, Mar. 2009. ISSN 00778923. doi: 10.1111/j.1749-6632.2009.04420.x.

C. Beckmann and S. Smith. Probabilistic Independent Component Analysis for Functional Magnetic Resonance Imaging. *IEEE Transactions on Medical Imaging*, 23(2):137–152, Feb. 2004. ISSN 0278-0062. doi: 10.1109/TMI.2003.822821.

C. Beckmann, C. Mackay, N. Filippini, and S. Smith. Group comparison of resting-state FMRI data using multi-subject ICA and dual regression. *NeuroImage*, 47:S148, July 2009. ISSN 10538119. doi: 10.1016/S1053-8119(09)71511-3.

C. F. Beckmann. Modelling with independent components. *NeuroImage*, 62(2):891–901, Aug. 2012. ISSN 10538119. doi: 10.1016/j.neuroimage.2012.02.020.

C. F. Beckmann, M. DeLuca, J. T. Devlin, and S. M. Smith. Investigations into resting-state connectivity using independent component analysis. *Philosophical Transactions of the Royal Society B: Biological Sciences*, 360(1457):1001–1013, May 2005. ISSN 0962-8436, 1471-2970. doi: 10.1098/rstb.2005.1634.

J. Bijsterbosch. *Introduction to Resting State fMRI Functional Connectivity*. Oxford Neuroimaging Primers. Oxford University Press, Oxford, United Kingdom ; New York, NY, first edition edition, 2017. ISBN 978-0-19-880822-0.

J. D. Bijsterbosch, M. W. Woolrich, M. F. Glasser, E. C. Robinson, C. F. Beckmann, D. C. Van Essen, S. J. Harrison, and S. M. Smith. The relationship between spatial configuration and functional connectivity of brain regions. *eLife*, 7:e32992, Feb. 2018. ISSN 2050-084X. doi: 10.7554/eLife.32992.

B. Biswal, F. Zerrin Yetkin, V. M. Haughton, and J. S. Hyde. Functional connectivity in the motor cortex of resting human brain using echo-planar mri. *Magnetic Resonance in Medicine*, 34(4):537–541, Oct. 1995. ISSN 07403194, 15222594. doi: 10.1002/mrm.1910340409.

J. Cabral, D. Vidaurre, P. Marques, R. Magalhães, P. Silva Moreira, J. Miguel Soares, G. Deco, N. Sousa, and M. L. Kringelbach. Cognitive performance in healthy older adults relates to spontaneous switching between states of functional connectivity during rest. *Scientific Reports*, 7(1):5135, Dec. 2017. ISSN 2045-2322. doi: 10.1038/s41598-017-05425-7.

V. Calhoun, T. Adali, G. Pearlson, and J. Pekar. Spatial and temporal independent component analysis of functional MRI data containing a pair of task-related waveforms.

Human Brain Mapping, 13(1):43–53, May 2001. ISSN 1065-9471, 1097-0193. doi: 10.1002/hbm.1024.

S. F. Cauley, J. R. Polimeni, H. Bhat, L. L. Wald, and K. Setsompop. Interslice leakage artifact reduction technique for simultaneous multislice acquisitions: Interslice Leakage Artifact Reduction Technique. *Magnetic Resonance in Medicine*, 72(1):93–102, July 2014. ISSN 07403194. doi: 10.1002/mrm.24898.

C. Chang and G. H. Glover. Time–frequency dynamics of resting-state brain connectivity measured with fMRI. *NeuroImage*, 50(1):81–98, Mar. 2010. ISSN 10538119. doi: 10.1016/j.neuroimage.2009.12.011.

J. S. Damoiseaux, S. A. R. B. Rombouts, F. Barkhof, P. Scheltens, C. J. Stam, S. M. Smith, and C. F. Beckmann. Consistent resting-state networks across healthy subjects. *Proceedings of the National Academy of Sciences*, 103(37):13848–13853, Sept. 2006. ISSN 0027-8424, 1091-6490. doi: 10.1073/pnas.0601417103.

J. S. Damoiseaux, K. E. Prater, B. L. Miller, and M. D. Greicius. Functional connectivity tracks clinical deterioration in Alzheimer's disease. *Neurobiology of Aging*, 33(4): 828.e19–828.e30, Apr. 2012. ISSN 01974580. doi: 10.1016/j.neurobiolaging.2011.06.024.

G. Deco and M. L. Kringelbach. Metastability and Coherence: Extending the Communication through Coherence Hypothesis Using A Whole-Brain Computational Perspective. *Trends in Neurosciences*, 39(3):125–135, Mar. 2016. ISSN 01662236. doi: 10.1016/j.tins.2016.01.001.

G. Deco, J. Cabral, M. W. Woolrich, A. B. Stevner, T. J. van Hartevelt, and M. L. Kringelbach. Single or multiple frequency generators in on-going brain activity: A mechanistic whole-brain model of empirical MEG data. *NeuroImage*, 152:538–550, May 2017. ISSN 10538119. doi: 10.1016/j.neuroimage.2017.03.023.

O. Esteban, C. J. Markiewicz, R. W. Blair, C. A. Moodie, A. I. Isik, A. Erramuzpe, J. D. Kent, M. Goncalves, E. DuPre, M. Snyder, H. Oya, S. S. Ghosh, J. Wright, J. Durnez, R. A. Poldrack, and K. J. Gorgolewski. fMRIPrep: A robust preprocessing pipeline for functional MRI. *Nature Methods*, 16(1):111–116, Jan. 2019. ISSN 1548-7091, 1548-7105.

V. Fonov, A. Evans, R. McKinstry, C. Almli, and D. Collins. Unbiased nonlinear average age-appropriate brain templates from birth to adulthood. *NeuroImage*, 47, 2009.

K. J. Friston. Modes or models: A critique on independent component analysis for fMRI. *Trends in Cognitive Sciences*, 2(10):373–375, Oct. 1998. ISSN 13646613. doi: 10.1016/S1364-6613(98)01227-3.

K. J. Friston, C. D. Frith, P. F. Liddle, and R. S. J. Frackowiak. Functional Connectivity: The Principal-Component Analysis of Large (PET) Data Sets. *Journal of Cerebral Blood Flow & Metabolism*, 13(1):5–14, Jan. 1993. ISSN 0271-678X, 1559-7016. doi: 10.1038/jcbfm.1993.4.

M. F. Glasser, T. S. Coalson, J. D. Bijsterbosch, S. J. Harrison, M. P. Harms, A. Anticevic, D. C. Van Essen, and S. M. Smith. Using temporal ICA to selectively remove global noise

while preserving global signal in functional MRI data. *NeuroImage*, 181:692–717, Nov. 2018. ISSN 10538119. doi: 10.1016/j.neuroimage.2018.04.076.

E. Glerean, J. Salmi, J. M. Lahnakoski, I. P. Jääskeläinen, and M. Sams. Functional Magnetic Resonance Imaging Phase Synchronization as a Measure of Dynamic Functional Connectivity. *Brain Connectivity*, 2(2):91–101, Apr. 2012. ISSN 2158-0014, 2158-0022. doi: 10.1089/brain.2011.0068.

D. E. Gomez, A. Llera, J. P. F. Marques, C. F. Beckmann, and D. G. Norris. Single-subject, Single-session, Temporal Modes of Brain Activity. *NeuroImage*, page 116783, May 2020. ISSN 10538119. doi: 10.1016/j.neuroimage.2020.116783.

K. J. Gorgolewski, T. Auer, V. D. Calhoun, R. C. Craddock, S. Das, E. P. Duff, G. Flandin, S. S. Ghosh, T. Glatard, Y. O. Halchenko, D. A. Handwerker, M. Hanke, D. Keator, X. Li, Z. Michael, C. Maumet, B. N. Nichols, T. E. Nichols, J. Pellman, J.-B. Poline, A. Rokem, G. Schaefer, V. Sochat, W. Triplett, J. A. Turner, G. Varoquaux, and R. A. Poldrack. The brain imaging data structure, a format for organizing and describing outputs of neuroimaging experiments. *Scientific Data*, 3(1):160044, Dec. 2016. ISSN 2052-4463. doi: 10.1038/sdata.2016.44.

M. D. Greicius, G. Srivastava, A. L. Reiss, and V. Menon. Default-mode network activity distinguishes Alzheimer's disease from healthy aging: Evidence from functional MRI. *Proceedings of the National Academy of Sciences*, 101(13):4637–4642, Mar. 2004. ISSN 0027-8424, 1091-6490. doi: 10.1073/pnas.0308627101.

M. D. Greicius, B. H. Flores, V. Menon, G. H. Glover, H. B. Solvason, H. Kenna, A. L. Reiss, and A. F. Schatzberg. Resting-State Functional Connectivity in Major Depression: Abnormally Increased Contributions from Subgenual Cingulate Cortex and Thalamus. *Biological Psychiatry*, 62(5):429–437, Sept. 2007. ISSN 00063223. doi: 10.1016/j.biopsych.2006.09.020.

D. N. Greve and B. Fischl. Accurate and robust brain image alignment using boundary-based registration. *NeuroImage*, 48(1):63–72, Oct. 2009. ISSN 10538119. doi: 10.1016/j.neuroimage.2009.06.060.

R. Hindriks, M. Adhikari, Y. Murayama, M. Ganzetti, D. Mantini, N. Logothetis, and G. Deco. Can sliding-window correlations reveal dynamic functional connectivity in resting-state fMRI? *NeuroImage*, 127:242–256, Feb. 2016. ISSN 10538119. doi: 10.1016/j.neuroimage.2015.11.055.

W. S. Hoge, K. Setsompop, and J. R. Polimeni. Dual-polarity slice-GRAPPA for concurrent ghost correction and slice separation in simultaneous multi-slice EPI. *Magnetic Resonance in Medicine*, 80(4):1364–1375, Oct. 2018. ISSN 07403194. doi: 10.1002/mrm.27113.

R. M. Hutchison, T. Womelsdorf, J. S. Gati, S. Everling, and R. S. Menon. Resting-state networks show dynamic functional connectivity in awake humans and anesthetized

macaques: Dynamic Functional Connectivity. *Human Brain Mapping*, 34(9):2154–2177, Sept. 2013. ISSN 10659471. doi: 10.1002/hbm.22058.

A. Hyvarinen. Fast and robust fixed-point algorithms for independent component analysis. *IEEE Transactions on Neural Networks*, 10(3):626–634, May 1999. ISSN 1045-9227, 1941-0093. doi: 10.1109/72.761722.

A. Iraji, A. Faghiri, N. Lewis, Z. Fu, S. Rachakonda, and V. Calhoun. Tools of the trade: Estimating time-varying connectivity patterns from fMRI data. Preprint, PsyArXiv, Mar. 2020.

M. Jenkinson, P. Bannister, M. Brady, and S. Smith. Improved Optimization for the Robust and Accurate Linear Registration and Motion Correction of Brain Images. *NeuroImage*, 17 (2):825–841, Oct. 2002. ISSN 10538119. doi: 10.1006/nimg.2002.1132.

M. Jenkinson, C. F. Beckmann, T. E. Behrens, M. W. Woolrich, and S. M. Smith. FSL. *NeuroImage*, 62(2):782–790, Aug. 2012. ISSN 10538119. doi: 10.1016/j.neuroimage.2011.09.015.

V. Kiviniemi, T. Vire, J. Remes, A. A. Elseoud, T. Starck, O. Tervonen, and J. Nikkinen. A Sliding Time-Window ICA Reveals Spatial Variability of the Default Mode Network in Time. *Brain Connectivity*, 1(4):339–347, Oct. 2011. ISSN 2158-0014, 2158-0022. doi: 10.1089/brain.2011.0036.

A. R. Laird, P. M. Fox, S. B. Eickhoff, J. A. Turner, K. L. Ray, D. R. McKay, D. C. Glahn, C. F. Beckmann, S. M. Smith, and P. T. Fox. Behavioral Interpretations of Intrinsic Connectivity Networks. *Journal of Cognitive Neuroscience*, 23(12):4022–4037, Dec. 2011. ISSN 0898-929X, 1530-8898.

C. Lanczos. Evaluation of Noisy Data. *Journal of the Society for Industrial and Applied Mathematics Series B Numerical Analysis*, 1(1):76–85, Jan. 1964. ISSN 0887-459X. doi: 10.1137/0701007.

M. Lehmann, C. Madison, P. M. Ghosh, Z. A. Miller, M. D. Greicius, J. H. Kramer, G. Coppola, B. L. Miller, W. J. Jagust, M. L. Gorno-Tempini, W. W. Seeley, and G. D. Rabinovici. Loss of functional connectivity is greater outside the default mode network in nonfamilial early-onset Alzheimer's disease variants. *Neurobiology of Aging*, 36(10): 2678–2686, Oct. 2015. ISSN 01974580. doi: 10.1016/j.neurobiolaging.2015.06.029.

N. Leonardi and D. Van De Ville. On spurious and real fluctuations of dynamic functional connectivity during rest. *NeuroImage*, 104:430–436, Jan. 2015. ISSN 10538119. doi: 10.1016/j.neuroimage.2014.09.007.

R. Liégeois, T. O. Laumann, A. Z. Snyder, J. Zhou, and B. T. Yeo. Interpreting Temporal Fluctuations in Resting-State Functional Connectivity MRI. Preprint, Neuroscience, May 2017.

R. Liégeois, J. Li, R. Kong, C. Orban, D. Van De Ville, T. Ge, M. R. Sabuncu, and B. T. T. Yeo. Resting brain dynamics at different timescales capture distinct aspects of human behavior. *Nature Communications*, 10(1):2317, Dec. 2019. ISSN 2041-1723. doi: 10.1038/s41467-019-10317-7.

X. Liu and J. H. Duyn. Time-varying functional network information extracted from brief instances of spontaneous brain activity. *Proceedings of the National Academy of Sciences*, 110(11):4392–4397, Mar. 2013. ISSN 0027-8424, 1091-6490. doi: 10.1073/pnas.1216856110.

A. Llera, R. Chauvin, P. Mulders, J. Naaijen, M. Mennes, and C. F. Beckmann. Spatial Patterns for Discriminative Estimation. *BioRxiv*, page 10, 2020.

D. J. Lurie, D. Kessler, D. S. Bassett, R. F. Betzel, M. Breakspear, S. Kheilholz, A. Kucyi, R. Liégeois, M. A. Lindquist, A. R. McIntosh, R. A. Poldrack, J. M. Shine, W. H. Thompson, N. Z. Bielczyk, L. Douw, D. Kraft, R. L. Miller, M. Muthuraman, L. Pasquini, A. Razi, D. Vidaurre, H. Xie, and V. D. Calhoun. Questions and controversies in the study of time-varying functional connectivity in resting fMRI. *Network Neuroscience*, 4(1):30–69, Jan. 2020. ISSN 2472-1751.

C. Lustig, A. Z. Snyder, M. Bhakta, K. C. O'Brien, M. McAvoy, M. E. Raichle, J. C. Morris, and R. L. Buckner. Functional deactivations: Change with age and dementia of the Alzheimer type. *Proceedings of the National Academy of Sciences*, 100(24):14504–14509, Nov. 2003. ISSN 0027-8424, 1091-6490. doi: 10.1073/pnas.2235925100.

M.-E. Lynall, D. S. Bassett, R. Kerwin, P. J. McKenna, M. Kitzbichler, U. Muller, and E. Bullmore. Functional Connectivity and Brain Networks in Schizophrenia. *Journal of Neuroscience*, 30(28):9477–9487, July 2010. ISSN 0270-6474, 1529-2401. doi: 10.1523/JNEUROSCI.0333-10.2010.

J. P. Marques, T. Kober, G. Krueger, W. van der Zwaag, P.-F. Van de Moortele, and R. Gruetter. MP2RAGE, a self bias-field corrected sequence for improved segmentation and T1-mapping at high field. *NeuroImage*, 49(2):1271–1281, Jan. 2010. ISSN 10538119. doi: 10.1016/j.neuroimage.2009.10.002.

M. McKeown. Independent component analysis of functional MRI: What is signal and what is noise? *Current Opinion in Neurobiology*, 13(5):620–629, Oct. 2003. ISSN 09594388. doi: 10.1016/j.conb.2003.09.012.

M. J. McKeown and T. J. Sejnowski. Independent component analysis of fMRI data: Examining the assumptions. *Human Brain Mapping*, page 5, 1998.

P. Mulders, A. Llera, I. Tendolkar, P. van Eijndhoven, and C. Beckmann. Personality Profiles Are Associated with Functional Brain Networks Related to Cognition and Emotion. *Scientific Reports*, 8(1):13874, Dec. 2018. ISSN 2045-2322. doi: 10.1038/s41598-018-32248-x.

P. C. Mulders, P. F. van Eijndhoven, A. H. Schene, C. F. Beckmann, and I. Tendolkar. Resting-state functional connectivity in major depressive disorder: A review. *Neuroscience*

& Biobehavioral Reviews, 56:330–344, Sept. 2015. ISSN 01497634. doi: 10.1016/j.neubiorev.2015.07.014.

R. K. Niazy, J. Xie, K. Miller, C. F. Beckmann, and S. M. Smith. Spectral characteristics of resting state networks. In *Progress in Brain Research*, volume 193, pages 259–276. Elsevier, 2011. ISBN 978-0-444-53839-0. doi: 10.1016/B978-0-444-53839-0.00017-X.

L. D. Nickerson, S. M. Smith, D. Öngür, and C. F. Beckmann. Using Dual Regression to Investigate Network Shape and Amplitude in Functional Connectivity Analyses. *Frontiers in Neuroscience*, 11, Mar. 2017. ISSN 1662-453X. doi: 10.3389/fnins.2017.00115.

S. Noteboom. *Ultrafast fMRI for Studying Ne Hemodynamic Response Latency Di Erences*. PhD thesis, University of Twente and Donders Institute, 2018.

N. Petridou, C. C. Gaudes, I. L. Dryden, S. T. Francis, and P. A. Gowland. Periods of rest in fMRI contain individual spontaneous events which are related to slowly fluctuating spontaneous activity. *Human Brain Mapping*, 34(6):1319–1329, June 2013. ISSN 10659471. doi: 10.1002/hbm.21513.

R. A. Poldrack, T. Nichols, and J. Mumford. *Handbook of Functional MRI Data Analysis*. Cambridge University Press, Cambridge, 2011. ISBN 978-0-511-89502-9. doi: 10.1017/CBO9780511895029.

M. G. Preti, T. A. Bolton, and D. Van De Ville. The dynamic functional connectome: State-of-the-art and perspectives. *NeuroImage*, 160:41–54, Oct. 2017. ISSN 10538119. doi: 10.1016/j.neuroimage.2016.12.061.

K. L. Ray, D. R. McKay, P. M. Fox, M. C. Riedel, A. M. Uecker, C. F. Beckmann, S. M. Smith, P. T. Fox, and A. R. Laird. ICA model order selection of task co-activation networks. *Frontiers in Neuroscience*, 7, 2013. ISSN 1662-453X. doi: 10.3389/fnins.2013.00237.

M. Reuter, H. D. Rosas, and B. Fischl. Highly accurate inverse consistent registration: A robust approach. *NeuroImage*, 53(4):1181–1196, Dec. 2010. ISSN 10538119. doi: 10.1016/j.neuroimage.2010.07.020.

B. P. Rogers, S. B. Katwal, V. L. Morgan, C. L. Asplund, and J. C. Gore. Functional MRI and multivariate autoregressive models. *Magnetic Resonance Imaging*, 28(8):1058–1065, Oct. 2010. ISSN 0730725X. doi: 10.1016/j.mri.2010.03.002.

M. J. Rosa, J. Daunizeau, and K. J. Friston. EEG-fMRI INTEGRATION: A CRITICAL REVIEW OF BIOPHYSICAL MODELING AND DATA ANALYSIS APPROACHES. *Journal of Integrative Neuroscience*, 09(04):453–476, Dec. 2010. ISSN 0219-6352, 1757-448X. doi: 10.1142/S0219635210002512.

C. Rosazza and L. Minati. Resting-state brain networks: Literature review and clinical applications. *Neurological Sciences*, 32(5):773–785, Oct. 2011. ISSN 1590-1874, 1590-3478. doi: 10.1007/s10072-011-0636-y.

K. Setsompop, B. A. Gagoski, J. R. Polimeni, T. Witzel, V. J. Wedeen, and L. L. Wald. Blipped-controlled aliasing in parallel imaging for simultaneous multislice echo planar imaging with reduced g -factor penalty: Blipped-CAIPI for Simultaneous Multislice EPI. *Magnetic Resonance in Medicine*, 67(5):1210–1224, May 2012. ISSN 07403194. doi: 10.1002/mrm.23097.

K. Singh and I. Fawcett. Transient and linearly graded deactivation of the human default-mode network by a visual detection task. *NeuroImage*, 41(1):100–112, May 2008. ISSN 10538119. doi: 10.1016/j.neuroimage.2008.01.051.

S. M. Smith, M. Jenkinson, M. W. Woolrich, C. F. Beckmann, T. E. Behrens, H. Johansen-Berg, P. R. Bannister, M. De Luca, I. Drobnjak, D. E. Flitney, R. K. Niazy, J. Saunders, J. Vickers, Y. Zhang, N. De Stefano, J. M. Brady, and P. M. Matthews. Advances in functional and structural MR image analysis and implementation as FSL. *NeuroImage*, 23:S208–S219, Jan. 2004. ISSN 10538119. doi: 10.1016/j.neuroimage.2004.07.051.

S. M. Smith, P. T. Fox, K. L. Miller, D. C. Glahn, P. M. Fox, C. E. Mackay, N. Filippini, K. E. Watkins, R. Toro, A. R. Laird, and C. F. Beckmann. Correspondence of the brain's functional architecture during activation and rest. *Proceedings of the National Academy of Sciences*, 106(31):13040–13045, Aug. 2009. ISSN 0027-8424, 1091-6490. doi: 10.1073/pnas.0905267106.

S. M. Smith, K. L. Miller, S. Moeller, J. Xu, E. J. Auerbach, M. W. Woolrich, C. F. Beckmann, M. Jenkinson, J. Andersson, M. F. Glasser, D. C. Van Essen, D. A. Feinberg, E. S. Yacoub, and K. Ugurbil. Temporally-independent functional modes of spontaneous brain activity. *Proceedings of the National Academy of Sciences*, 109(8):3131–3136, Feb. 2012. ISSN 0027-8424, 1091-6490. doi: 10.1073/pnas.1121329109.

E. Tagliazucchi, M. Siniatchkin, H. Laufs, and D. R. Chialvo. The Voxel-Wise Functional Connectome Can Be Efficiently Derived from Co-activations in a Sparse Spatio-Temporal Point-Process. *Frontiers in Neuroscience*, 10, Aug. 2016. ISSN 1662-453X. doi: 10.3389/fnins.2016.00381.

J. M. Treiber, N. S. White, T. C. Steed, H. Bartsch, D. Holland, N. Farid, C. R. McDonald, B. S. Carter, A. M. Dale, and C. C. Chen. Characterization and Correction of Geometric Distortions in 814 Diffusion Weighted Images. *PLOS ONE*, 11(3):e0152472, Mar. 2016. ISSN 1932-6203.

N. J. Tustison, B. B. Avants, P. A. Cook, Yuanjie Zheng, A. Egan, P. A. Yushkevich, and J. C. Gee. N4ITK: Improved N3 Bias Correction. *IEEE Transactions on Medical Imaging*, 29(6):1310–1320, June 2010. ISSN 0278-0062, 1558-254X. doi: 10.1109/TMI.2010.2046908.

L. Q. Uddin. Typical and atypical development of functional human brain networks: Insights from resting-state fMRI. *Frontiers in Systems Neuroscience*, 4, 2010. ISSN 16625137. doi: 10.3389/fnsys.2010.00021.

E. van Oort, P. Koopmans, R. Boyacioglu, M. Barth, C. Beckmann, and D. Norris. Frequency characteristics of large scale resting state networks using 7T Spin Echo EPI. *Proc. Intl. Soc. Mag. Reson. Med.*, page 1, 2012.

E. S. van Oort, M. Mennes, T. Navarro Schröder, V. J. Kumar, N. I. Zaragoza Jimenez, W. Grodd, C. F. Doeller, and C. F. Beckmann. Functional parcellation using time courses of instantaneous connectivity. *NeuroImage*, 170:31–40, Apr. 2018. ISSN 10538119. doi: 10.1016/j.neuroimage.2017.07.027.

D. Vidaurre, A. J. Quinn, A. P. Baker, D. Dupret, A. Tejero-Cantero, and M. W. Woolrich. Spectrally resolved fast transient brain states in electrophysiological data. *NeuroImage*, 126: 81–95, Feb. 2016. ISSN 10538119. doi: 10.1016/j.neuroimage.2015.11.047.

D. Vidaurre, S. M. Smith, and M. W. Woolrich. Brain network dynamics are hierarchically organized in time. *Proceedings of the National Academy of Sciences*, 114(48):12827–12832, Nov. 2017. ISSN 0027-8424, 1091-6490. doi: 10.1073/pnas.1705120114.

S. Wang, D. J. Peterson, J. C. Gatenby, W. Li, T. J. Grabowski, and T. M. Madhyastha. Evaluation of Field Map and Nonlinear Registration Methods for Correction of Susceptibility Artifacts in Diffusion MRI. *Frontiers in Neuroinformatics*, 11, Feb. 2017. ISSN 1662-5196. doi: 10.3389/fninf.2017.00017.

M. Yaesoubi, E. A. Allen, R. L. Miller, and V. D. Calhoun. Dynamic coherence analysis of resting fMRI data to jointly capture state-based phase, frequency, and time-domain information. *NeuroImage*, 120:133–142, Oct. 2015. ISSN 10538119. doi: 10.1016/j.neuroimage.2015.07.002.

Y. Zhang, M. Brady, and S. Smith. Segmentation of brain MR images through a hidden Markov random field model and the expectation-maximization algorithm. *IEEE Transactions on Medical Imaging*, 20(1):45–57, Jan./2001. ISSN 02780062. doi: 10.1109/42.906424.

6 Supplementary Material

I. Data and code availability statement

Data will be stored at the Donders Repository, and are made available upon request. A documented python package was developed for TV-TFM analysis, which will be made available under https://github.com/tamarajedidja/tv-tfm upon publication. The package only supports python 3.6+.

II. Dataset selection

A single-subject, single task-run dataset was selected for illustrative purposes. This dataset was initially selected based on the numbers of spatial correlations larger than $r = .3$ (an arbitrary threshold), between the well-defined networks of the SMITH20 template and TFMs (see Table 2). Given the assumption of the model that temporal ICA at stage two of the analysis needs to adequately identify the process of interest, we selected the TFMs that were most strongly associated with the visual task regressors and correlated those to the task. Of the participants for which all three sessions were included, the correlation between the TFM that showed the strongest absolute correlation with the visual task regressor and the task regressor, was strongest for the selected dataset ($r = .48$; visually presented for all task-runs in panel B of Figure 12).

Table 2
Spatial correlations between the SMITH20 and TFMs.

Participant	Descriptives	
	Range	No. of $r > 0.3$ (ses-01,02,03)*
1	<0.001–0.38	3, 2, 4
2	0.001–0.41	2, 2, 3
3	<0.001–0.42	3, 4, 2
4	<0.001–0.48	3, 4, 4
5	<0.001–0.40	2, 0, 4
6	<0.001–0.31	0, 7, 3
7	<0.001–0.34	2, 1, 3
8	0.001–0.30	0, 1
9	<0.001–0.45	3, 4, **8**
10	<0.001–0.34	2, 2, 4
11	0.001–0.38	2, 3, 4
12	0.001–0.44	2, 6
13	0.001–0.41	2, 3, 1
14	<0.001–0.45	6, 7, 2

* Number of correlations between the **well-defined** networks of the SMITH20 template and TFMs that are larger than $r = .3$.

III. Stage 1 dual-regression: statistics one-sample *t*-tests

To identify the dual-regression time series that across participants were significantly related to the task, a third-level analysis was performed using a one-sample *t*-test per resting-state network as identified by Smith et al. (2009). An overview of the Bonferroni corrected *t*-statistics is presented in Table 3.

Table 3
Group-level results: one-sample t-test on Fisher-Z transformed correlations of task vs. DR time series.

Participant	Descriptives			
	Visual		Motor	
	t-value	*p*-value	*t*-value	*p*-value
Primary visual (V2)**	0.63	0.5366	-2.87	0.0132
Lateral visual (V3)**	7.43	< 0.0001*	0.96	0.3530
Medial visual (V1)**	5.45	0.0001*	6.34	< 0.0001*
Sensorimotor**	8.59	< 0.0001*	3.30	0.0057
Cerebellum**	-10.94	< 0.0001*	-6.97	< 0.0001*
Auditory**	10.67	< 0.0001*	8.52	< 0.0001*
ECN**	-0.93	0.3671	-0.52	0.6145
Frontoparietal (Left)**	3.93	0.0017*	5.62	< 0.0001*
Frontoparietal (Right)**	4.74	0.0004*	8.25	< 0.0001*
DMN**	-9.58	< 0.0001*	-7.52	< 0.0001*
NWD (Hippocampal)	0.65	0.5244	1.16	0.2660
NWD (IFG and Amygdala)	-11.08	< 0.0001*	-8.67	< 0.0001*
NWD (Insula network)	-0.19	0.8530	-0.63	0.5387
NWD (1)	-6.04	< 0.0001*	-5.04	0.0002*
NWD (2)	-5.88	< 0.0001*	-6.27	< 0.0001*
NWD (3)	-8.55	< 0.0001*	-10.54	< 0.0001*
NWD (4)	4.99	.0002*	6.88	< 0.0001*
NWD (5)	-3.44	.0044*	-3.14	0.007
NWD (6)	0.40	.6965	2.12	0.0537
NWD (7)	4.17	.0011*	4.42	0.0007*

(**) Well-defined Smith network; NWD = not well-defined;
(*) Significantly different from zero, after Bonferroni correction (i.e. significance below .05/20 = .0025)

IV. Stage 2 classical TFM: correlation to confounds

TFM time series were correlated to confound time series as an indication of their neuronal basis. Figure 20 presents the resulting correlation matrix for the selected dataset in panel A. As described in the main manuscript, group-level comparisons per TFM are problematic due to the correspondence problem of temporal ICA. Therefore, TFM time series that showed the strongest absolute correlation to the task regressors were selected, and were correlated with the confound regressors. The Fisher-Z transformed correlation values are presented for all task-runs and participants in panel B of Figure 20. Evident from this picture is the enlarged associations with the global signal. This finding is in line with the conclusion by Glasser et al. (2018), that spatial ICA (as used for data cleaning in the current study) is very effective at removing spatially specific structured noise from high temporal resolution fMRI data, but that it can not selectively and completely remove global structured noise while retaining global signal form neural activity. Clean up using temporal ICA was proposed as a potential solution, which could be considered in the future.

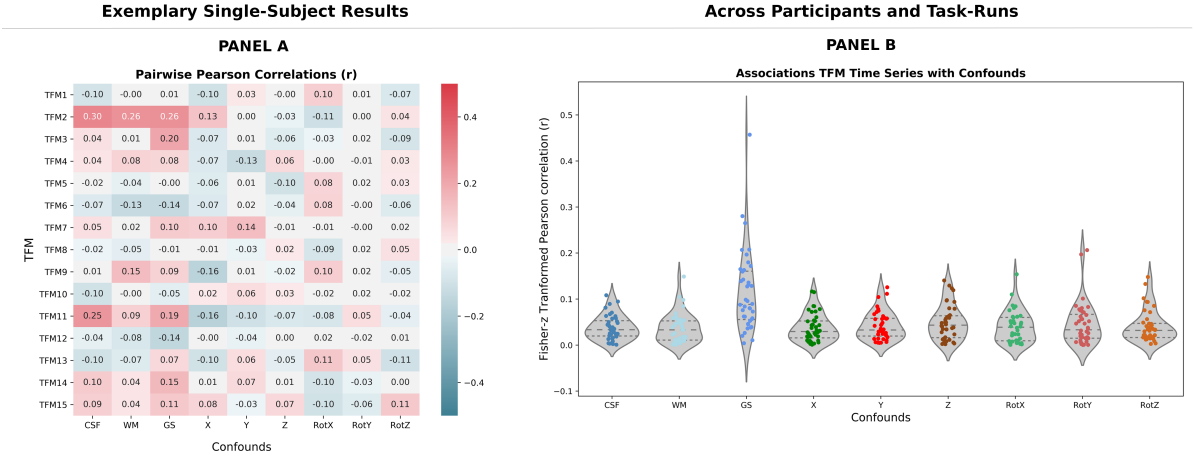

Figure 20. Panel A shows an example of the correlation matrix between all TFM time series and the confound regressors, illustratively for the selected dataset. Panel B shows the distributions of the Fisher-Z transformed correlation values between the TFM time series that correlated most strongly with the visual task regressor and the confound regressors, per task-run.

V. Stage 2 classical TFM: identified TFMs

TFMs similar to the task-positive mode and default temporal mode as identified for the selected dataset were found across most participants and task-runs. Pairwise Pearson correlations between the node weights of M for these TFMs as identified for the selected dataset and the node weights of all other extracted TFMs were computed per task-run. Distributions of the strongest absolute correlations per task-run are plotted in Figure 21.

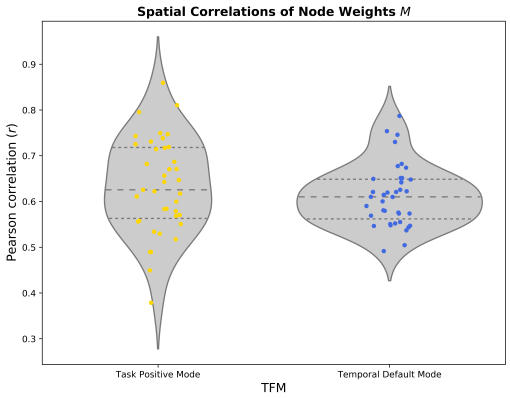

Figure 21. Spatial (node weight) correlations per task-run, for the TFM which showed the strongest absolute correlation with the task-positive mode on the left, and for the TFM which showed the strongest absolute correlation with the default temporal mode on the right.

In Figure 22 two illustrative spatial maps are plotted for the TFMs that correlated most strongly to the task-positive mode as identified for the selected dataset, and two illustrative spatial maps are plotted for the TFMs that correlated most strongly to the default temporal mode as identified for the selected dataset.

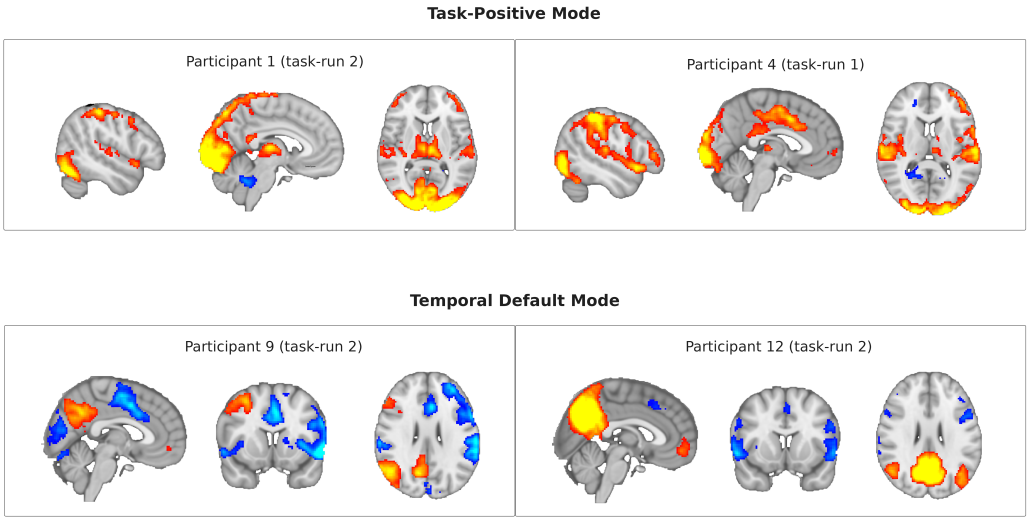

Figure 22. Representative examples of TFMs similar to the task-positive mode and the default temporal mode as identified for the selected dataset. In the top panel: the two TFMs that correlated most strongly to the task-positive mode, as identified for the selected dataset. In the bottom panel: the two TFMs that correlated most strongly to the default temporal mode, as identified for the selected dataset.

VI. Stage 2 classical TFM: Default temporal mode for temporal ICA model-order 10

In Figure 23 the spatial map of the default temporal mode is presented for the selected dataset, as obtained with a temporal ICA of model-order ten on the time series of the ten-well defined networks by Smith et al. (2009). We observe that at this model-order, the default temporal mode involves an anti-correlated pattern between core hubs of the DMN *also in anti-correlation with visual areas.*

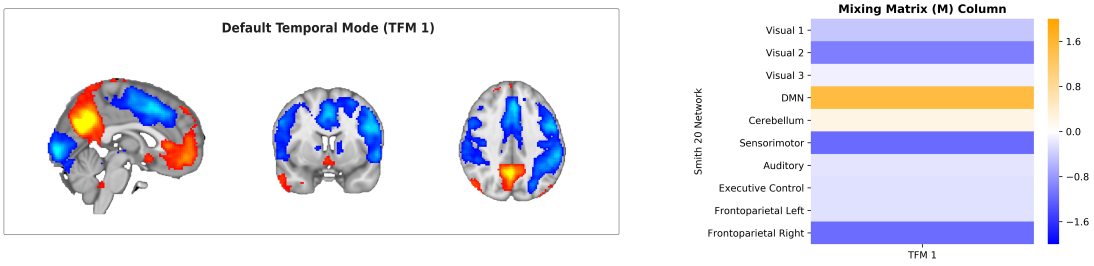

Figure 23. Three representative slices of the default temporal mode for the selected dataset after temporal ICA with a model-order of ten (TFM1; thresholded at $Z > 5$), and the associated mixing matrix column.

VII. Stage 3 TV-TFM: correlation values for all entries of f per TFM

Results presented in Table 4 show that the sum of the absolute correlation values across the entries of f for each TFM, for associations of entries of f with the visual and motor task regressors. We observed that the sum of the correlation values was highest for TFM3 when related to the visual task regressor, and for entries of TFM14 when related to the motor task regressor (for the selected dataset). These were the same TFMs for which the time series correlated most strongly to the task regressors.

Table 4
Sum of the absolute correlation values for all entries of f per TFM

TFM	Sum of the absolute r-values:	
	Visual	Motor
TFM1	1.33	0.92
TFM2	1.20	1.03
TFM3	3.83	1.69
TFM4	1.16	1.10
TFM5	1.74	1.35
TFM6	1.59	2.04
TFM7	1.09	0.98
TFM8	1.53	1.80
TFM9	0.96	0.92
TFM10	0.80	0.86
TFM11	0.54	1.03
TFM12	1.22	1.49
TFM13	1.35	0.95
TFM14	1.38	2.33
TFM15	0.94	0.93

VIII. Stage 3 TV-TFM: Trial-averaged entries of f per task-run, per-participant.

We observed a pattern in the time-varying mixing matrix entries of the task-positive mode for the selected dataset that closely followed the task-design. A similar trend was observed for most participants and task-runs, which are presented in Figure 24. This figure shows the trial-averaged task-relevant entries of f for the TFM that was most strongly associated with the visual task regressor per task-run, per participant.

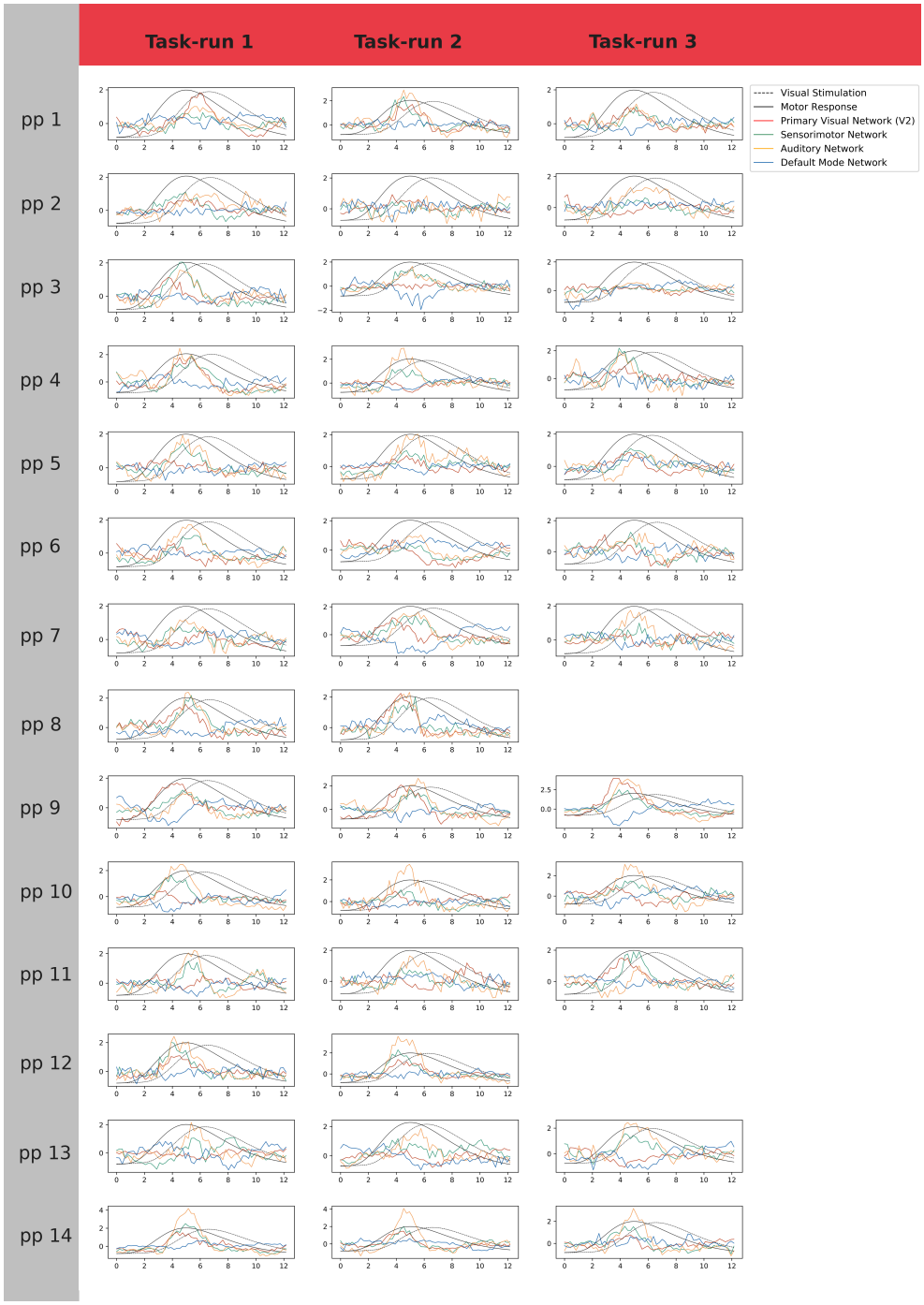

Figure 24. Trial-averaged entries of f for the task-relevant networks for the TFM which showed the strongest absolute correlation with the visual task regressor, per task-run, per participant.

7 Acknowledgements

I would like to thank several people that made this thesis possible. First of all, I would like to thank Alberto, who not only came up with the initial idea and the derivation for this "Moonshine" method but with whom I went through all the ups and downs of the development process. Thank you for trusting me with it, for the endlessly interesting and fun discussions, and for deliberating the most complicated material with me at one moment and just as patiently explaining something basic the next. A major thanks also to Christian, who welcomed me into his lab group with open arms, who only needs a split second to hit the nail on the head, and gives spot-on feedback. Thank you for your concern for my wellbeing, facilitating Toolkits and courses, and for the fun talks. Thirdly, Nils: thank you for your consistency in meeting with me during quarantine, your feedback, and the interesting (project-related and other) discussions. I'm looking forward to the next four years. I would also like to thank my RetteRetraite team, Tim, Lotje, Christl, Gerwin and Yentl, who prevented lonely working days in quarantine and gave structure to my working days, and to Fonti who provided me with a working space and "oat cappuccinos" . Thank you Christl and Yentl for always being there, monitoring my well-being, and celebrating all highs and lows. I'd also like to kindly thank my parents, who have always supported me in many more ways than I can express in words, and who have taught me to use my abilities for a greater good. And last, but not least: Djarno, my love. Thank you for the wonderful, stable force you are in my life. For the desk you build me, and the endless meals you prepared. For smiling when my hyperfocus prevents me from paying attention to my immediate surroundings, or when I stumble over my own feet because my mind is solving problems. I couldn't have done it, but more importantly, I wouldn't have wanted to do it without all of you!